1  Present and future aerosol impacts on Arctic climate change in the GISS-E2.1 Earth system
2  model

4  Ulas Im[1,2,*], Kostas Tsigaridis[3,4], Gregory Faluvegi[3,4], Peter L. Langen[1,2], Joshua P. French[5],
5  Rashed Mahmood[6], Manu A. Thomas[7], Knut von Salzen[8], Daniel C. Thomas[1,2], Cynthia H.
6  Whaley[8], Zbigniew Klimont[9], Henrik Skov[1,2], Jørgen Brandt[1,2]
7
8  [1]Department of Environmental Science, Aarhus University, Roskilde, Denmark.
9  [2] Interdisciplinary Centre for Climate Change, Aarhus University, Roskilde, Denmark.
10 [3] Center for Climate Systems Research, Columbia University, New York, NY, USA.
11 [4] NASA Goddard Institute for Space Studies, New York, NY, USA.
12 [5] Department of Mathematical and Statistical Sciences, University of Colorado Denver, USA.
13 [6] Barcelona Supercomputing Center,  Barcelona, Spain.
14 [7] Swedish Meteorological and Hydrological Institute, Norrköping, Sweden.
15 [8] Canadian Centre for Climate Modelling and Analysis, Environment and Climate Change Canada,
16 Victoria, British Columbia, Canada.
17 [9] International Institute for Applied Systems Analysis (IIASA), Laxenburg, Austria.
18 [*] Corresponding author

20 Abstract

22 The Arctic is warming two to three times faster than the global average, partly due to changes
23 in short-lived climate forcers (SLCFs) including aerosols. In order to study the effects of
24 atmospheric aerosols in this warming, recent past (1990-2014) and future (2015-2050)
25 simulations have been carried out using the GISS-E2.1 Earth system model to study the
26 aerosol burdens and their radiative and climate impacts over the Arctic (>60 °N), using
27 anthropogenic emissions from the Eclipse V6b and the Coupled Model Intercomparison
28 Project Phase 6 (CMIP6) databases, while global annual mean greenhouse gas concentrations
29 were prescribed and kept fixed in all simulations.
30
31 Results showed that the simulations have underestimated observed surface aerosol levels, in
32 particular black carbon (BC) and sulfate ($SO_4^{2-}$), by more than 50%, with the smallest biases
33 calculated for the atmosphere-only simulations, where winds are nudged to reanalysis data.
34 CMIP6 simulations performed slightly better in reproducing the observed surface aerosol
35 concentrations and climate parameters, compared to the Eclipse simulations. In addition,
36 simulations, where atmosphere and ocean are fully-coupled, had slightly smaller biases in
37 aerosol levels compared to atmosphere only simulations without nudging.
38
39 Arctic BC, organic aerosol (OA) and $SO_4^{2-}$ burdens decrease significantly in all simulations
40 by 10-60% following the reductions of 7-78% in emission projections, with the Eclipse
41 ensemble showing larger reductions in Arctic aerosol burdens compared to the CMIP6
42 ensemble. For the 2030-2050 period, the Eclipse ensemble simulated a radiative forcing due
43 to aerosol-radiation interactions ($RF_{ARI}$) of -0.39±0.01 W m$^{-2}$, that is -0.08 W m$^{-2}$ larger than
44 the 1990-2010 mean forcing (-0.32 W m$^{-2}$), of which -0.24±0.01 W m$^{-2}$ were attributed to the
45 anthropogenic aerosols. The CMIP6 ensemble simulated a $RF_{ARI}$ of -0.35 to -0. 40 W m$^{-2}$ for

46  the same period, which is -0.01 to -0.06 W m$^{-2}$ larger than the 1990-2010 mean forcing of -

47  0.35 W m$^{-2}$. The scenarios with little to no mitigation (worst-case scenarios) led to very small

48  changes in the RF$_{ARI}$, while scenarios with medium to large emission mitigations led to

49  increases in the negative RF$_{ARI}$, mainly due to the decrease of the positive BC forcing and the

50  decrease in the negative SO$_4^{2-}$ forcing. The anthropogenic aerosols accounted for -0.24 to -

51  0.26 W m$^{-2}$ of the net RF$_{ARI}$ in 2030-2050 period, in Eclipse and CMIP6 ensembles,

52  respectively. Finally, all simulations showed an increase in the Arctic surface air

53  temperatures throughout the simulation period. By 2050, surface air temperatures are

54  projected to increase by 2.4 °C to 2.6 °C in the Eclipse ensemble and 1.9 °C to 2.6 °C in the

55  CMIP6 ensemble, compared to the 1990-2010 mean.

56

57  Overall, results show that even the scenarios with largest emission reductions leads to similar

58  impact on the future Arctic surface air temperatures and sea-ice extent compared to scenarios

59  with smaller emission reductions, implying reductions of greenhouse emissions are still

60  necessary to mitigate climate change.

61

62  1.      Introduction

63

64  The Arctic is warming two to three times faster than the global average (IPCC, 2013;

65  Lenssen et al., 2019). This is partly due to internal Arctic feedback mechanisms, such as the

66  snow and sea-ice-albedo feedback, where melting ice leads to increased absorption of solar

67  radiation, which further enhances warming in the Arctic (Serreze and Francis, 2006).

68  However, Arctic temperatures are also affected by interactions with warming at lower

69  latitudes (e.g., Stuecker et al., 2018; Graversen and Langen, 2019; Semmler et al., 2020) and

70  by local in situ response to radiative forcing due to changes in greenhouse gases and aerosols

71  in the area (Shindell, 2007; Stuecker et al., 2018). In addition to warming induced by

72  increases in global atmospheric carbon dioxide (CO$_2$) concentrations, changes in short-lived

73  climate forcers (SLCFs) such as tropospheric ozone (O$_3$), methane (CH$_4$) and aerosols (e.g.

74  black carbon (BC) and sulfate (SO$_4^{2-}$)) in the Northern Hemisphere (NH), have contributed

75  substantially to the Arctic warming since 1890 (Shindell and Faluvegi, 2009; Ren et al.,

76  2020). This contribution from SLCFs to Arctic heating together with efficient local

77  amplification mechanisms puts a high priority on understanding the sources and sinks of

78  SLCFs at high latitudes and their corresponding climatic effects.

79

80  SLCFs include all atmospheric species, which have short residence times in the atmosphere

81  relative to long-lived greenhouse gases and have the potential to affect Earth's radiative

82  energy budget. Aerosols are important SLCFs and are a predominant component of air

83  quality that affects human health (Burnett et al., 2018, Lelieveld et al., 2019). They mostly

84  affect climate by altering the amount of solar energy absorbed by Earth, as well as changing

85  the cloud properties and indirectly affecting the scattering of radiation, and are efficiently

86  removed from the troposphere within several days to weeks. BC, which is a product of

87  incomplete combustion and open biomass/biofuel burning (Bond et al., 2004: 2013), absorbs

88  a high proportion of incident solar radiation and therefore warms the climate system

89  (Jacobson, 2001). SO$_4^{2-}$, which is formed primarily through oxidation of sulphur dioxide

90  (SO$_2$), absorbs negligible solar radiation and cools climate by scattering solar radiation back
91  to space. Organic carbon (OC), which is co-emitted with BC during combustion, both scatters
92  and absorbs solar radiation and therefore causes cooling in some environments and warming
93  in others. Highly reflective regions such as the Arctic are more likely to experience warming
94  effects from these organic aerosols (e.g., Myhre et al, 2013).
95
96  Aerosols also influence climate via indirect mechanisms. After being deposited on snow and
97  ice surfaces, BC can amplify ice melt by lowering the albedo and increasing solar heating of
98  the surface (AMAP, 2015). Aerosols also affect cloud properties, including their droplet size,
99  lifetime, and vertical extent, thereby influencing both the shortwave cooling and longwave
100  warming effects of clouds. Globally, this indirect cloud forcing from aerosols is likely larger
101  than their direct forcing, although the indirect effects are more uncertain and difficult to
102  accurately quantify (IPCC, 2013). Moreover, Arctic cloud impacts are distinct from global
103  impacts, owing to the extreme seasonality of solar radiation in the Arctic, unique
104  characteristics of Arctic clouds (e.g., high frequency of mixed-phase occurrence), and rapidly
105  evolving sea-ice distributions. Together, they lead to complicated and unique phenomena that
106  govern Arctic aerosol abundances and climate impacts (e.g., Willis et al., 2018; Abbatt et al.,
107  2019). The changes taking place in the Arctic have consequences for how SLCFs affect the
108  region. For example, reductions in sea-ice extent, thawing of permafrost, and humidification
109  of the Arctic troposphere can affect the emissions, lifetime and radiative forcing of SLCFs
110  within the Arctic (Thomas et al., 2019).
111
112  The effect of aerosols on the Arctic climate through the effects of scattering and absorption of
113  radiation, clouds, and surface ice/snow albedo has been investigated in previous studies (i.e.
114  Clarke and Noone, 1985; Flanner et al., 2007; Shindell et al., 2012; Bond et al., 2013;
115  Dumont et al., 2014). The impact of aerosols on the Arctic climate change is mainly driven
116  by a response to remote forcings (Gagné et al., 2015; Sand et al., 2015; Westervelt et al.,
117  2015). Long-range transport is known to play an important role in the Arctic air pollution
118  levels and much of the attention on aerosol climatic effects in the Arctic was focused on
119  long-range transported anthropogenic pollution (Arctic haze) in the past (Quinn et al., 2017;
120  AMAP, 2015; Abbatt et al., 2019).  Long-range transport of BC and SO$_4^{2-}$, in particular from
121  Asia, travelling at a relatively high altitude to the Arctic, can be deposited on the snow and
122  ice, contributing to surface albedo reduction. On the other hand, there has been increasing
123  attention on the local Arctic aerosol sources, in particular natural aerosol sources (Schmale et
124  al., 2021). Lewinschal et al. (2019) estimated an Arctic surface temperature change per unit
125  global sulfur emission of -0.020 to -0.025 K per TgS yr$^{-1}$. Sand et al. (2020) calculated an
126  Arctic surface air temperature response of 0.06 - 0.1 K per Tg BC yr$^{-1}$ to BC emissions in
127  Europe and North America, and slightly lower response (0.05-0.08 K per Tg BC yr$^{-1}$) to
128  Asian emissions. Breider et al. (2017) reported a short-wave (SW) aerosol radiative forcing
129  (ARF) of $-0.19 \pm 0.05$ W m$^{-2}$ at the top of the atmosphere (TOA) over the Arctic, which
130  reflects the balance between sulphate cooling ($-0.60$ W m$^{-2}$) and black carbon (BC) warming
131  ($+0.44$ W m$^{-2}$). Schacht et al. (2019) calculated a direct radiative forcing of up to 0.4 W m$^{-2}$
132  over the Arctic using the ECHAM6.3-HAM2.3 global aerosol-climate model. Markowicz et
133  al. (2021), using the NAAPS radiative transfer model, calculated the total aerosol forcing

over the Arctic (>70.5 °N) of -0.4 W m$^{-2}$. Ren et al. (2020) simulated 0.11 and 0.25 W m$^{-2}$ direct and indirect warming in 2014-2018 compared to 1980-1984 due to reductions in sulfate, using the CAM5-EAST global aerosol-climate model. They also reported that the aerosols produced an Arctic surface warming of +0.30 °C during 1980–2018, explaining about 20% of the observed Arctic warming observed during the last four decades, while according to Shindell and Faluvegi (2009), aerosols contributed 1.09 ± 0.81 °C to the observed Arctic surface air temperature increase of 1.48 ± 0.28 °C observed in 1976-2007. AMAP (2015), based on four ESMs, estimated a total Arctic surface air temperature response due to the direct effect of current global combustion derived BC, OC and sulfur emissions to be +0.35 °C, of which +0.40 °C was attributed to BC in the atmosphere, +0.22 °C to BC in snow, -0.04 °C to OC and -0.23 °C to $SO_4^{2-}$. On the other hand, Stjern et al. (20117) and Takemura and Suzuki (2019) showed that due to the rapid adjustments from BC, mitigation of BC emissions can lead to weak responses in the surface temperatures. Samset et al. (2018), using a multi-model ensemble of ocean coupled Earth system models (ESMs), where aerosol emissions were either kept at present-day conditions, or anthropogenic emissions of $SO_2$, and fossil fuel BC and OC were set to zero, showed that Arctic surface warming due to aerosol reductions can reach up to  4°C in some locations, with a multi-model increase for the 60°N–90°N region being 2.8°C. In addition, recent studies also suggest that as global emissions of anthropogenic aerosols decrease, natural aerosol feedbacks may become increasingly important for Arctic climate (Boy et al., 2019; Mahmood et al., 2019).

In this study, we carry out several simulations with the fully coupled NASA Goddard Institute of Space Sciences (GISS) earth system model, GISS-E2.1 (Kelley et al., 2020) to study the recent past and future burdens of aerosols as well as their impacts on TOA radiative forcing and climate-relevant parameters such as surface air temperatures, sea-ice, and snow over the Arctic (>60 °N). In addition, we investigate the impacts from two different emission inventories; Eclipse V6b (Höglund-Isaksson et al.,2020; Klimont et al., 2021) vs. CMIP6 (Hoesly et al., 2018; van Marle et al., 2017: Feng et al., 2020), as well as differences between atmosphere-only vs. fully-coupled simulations, on the evaluation of the model and the climate impact. Section 2 introduces the GISS-E2.1 model, the anthropogenic emissions, and the observation datasets used in model evaluation. Section 3 presents results from the model evaluation as well as recent past and future trends in simulated aerosol burdens, radiative forcing, and climate change over the Arctic. Section 4 summarizes the overall findings and the conclusions.

2.    Materials and methods

2.1.    Model description

GISS-E2.1 is the CMIP6 version of the GISS modelE Earth system model, which has been validated extensively over the globe (Kelly et al., 2020; Bauer et al., 2020) as well as regionally for air pollutants (Turnock et al., 2020). A full description of GISS-E2.1 and evaluation of its coupled climatology during the satellite era (1979–2014) and the recent past ensemble simulation of the atmosphere and ocean component models (1850-2014) are

178 described in Kelly et al. (2020) and Miller et al. (2020), respectively. GISS-E2.1 has a
179 horizontal resolution of 2° in latitude by 2.5° in longitude and 40 vertical layers extending
180 from the surface to 0.1 hPa in the lower mesosphere. The tropospheric chemistry scheme
181 used in GISS-E2.1 (Shindell et al., 2013) includes inorganic chemistry of $O_x$, $NO_x$, $HO_x$, CO,
182 and organic chemistry of $CH_4$ and higher hydrocarbons using the CBM4 scheme (Gery et al.,
183 1989), and the stratospheric chemistry scheme (Shindell et al., 2013), which includes chlorine
184 and bromine chemistry together with polar stratospheric clouds.
185
186 In the present work, we used the One-Moment Aerosol scheme (OMA: Bauer et al., 2020 and
187 references therein), which is a mass-based scheme in which aerosols are assumed to remain
188 externally mixed. All aerosols have a prescribed and constant size distribution, with the
189 exception of sea salt that has two distinct size classes, and dust that is described by a
190 sectional model with an option from 4 to 6 bins. The default dust configuration that is used in
191 this work includes 5 bins, a clay and 4 silt ones, from submicron to 16 μm in size. The first
192 three dust size bins can be coated by sulfate and nitrate aerosols (Bauer & Koch, 2005). The
193 scheme treats sulfate, nitrate, ammonium, carbonaceous aerosols (black carbon and organic
194 carbon, including the $NO_x$-dependent formation of secondary organic aerosol (SOA) and
195 methanesulfonic acid formation), dust and sea-salt. The model includes secondary organic
196 aerosol production, as described by Tsigaridis and Kanakidou, (2007). SOA is calculated
197 from terpenes and other reactive volatile organic compounds (VOCs) using NOx-dependent
198 calculations of the 2-product model, as described in Tsigaridis and Kanakidou (2007).
199 Isoprene is explicitly used as a source, while terpenes and other reactive VOCs are lumped on
200 a-pinene, taking into account their different reactivity against oxidation. The semi-volatile
201 compounds formed can condense on all submicron particles except sea salt and dust. In the
202 model, an OA to OC ratio of 1.4 used. OMA only includes the first indirect effect, in which
203 the aerosol number concentration that impacts clouds is obtained from the aerosol mass as
204 described in (Menon & Rotstayn, 2006). The parameterization described by Menon and
205 Rotstayn (2006) that we use only affects the cloud droplet number concentration (CDNC),
206 not cloud droplet size, which is not explicitly calculated in GISS-E2.1. Following the change
207 in CDNC, we do not stop the model from changing either liquid water path (LWP) or
208 precipitation rates, since the clouds code sees the different CDNC and responds accordingly.
209 What we do not include is the 2nd indirect effect (autoconversion). In addition to OMA, we
210 have also conducted a non-interactive tracers (NINT: Kelley et al., 2020) simulation from
211 1850 to 2014, with noninteractive (through monthly varying) fields of radiatively active
212 components (ozone and multiple aerosol species) read in from previously calculated offline
213 fields from the OMA version of the model, ran using the Atmospheric Model
214 Intercomparison Project (AMIP) configuration in Bauer et al. (2020) as described in Kelley et
215 al. (2020). The NINT model includes a tuned aerosol first indirect effect following Hansen et
216 al. (2005).
217
218 The natural emissions of sea salt, dimethylsulfide (DMS), isoprene and dust are calculated
219 interactively. Anthropogenic dust sources are not represented in GISS-E2.1. Dust emissions
220 vary spatially and temporally only with the evolution of climate variables like wind speed
221 and soil moisture (Miller et al., 2006). Dust concentrations are tuned to match the observed

dust aerosol optical depth (AOD). The AMIP type simulations (see section 2.3) uses prescribed sea surface temperature (SST) and sea ice fraction during the recent past (Rayner et al., 2003). The prescribed SST dataset in GISS-E2.1 is merged product based on the HadISST and NOAA Optimum Interpolation (OI) Sea Surface Temperature (SST) V2 (Reynolds et al., 2002).

## 2.2. Emissions

In this study, we have used two different emission datasets; the ECLIPSE V6b (Höglund-Isaksson et al.,2020; Klimont et al., 2021), which has been developed with support of the EU-funded Action on Black Carbon in the Arctic (EUA-BCA) and used in the framework of the ongoing AMAP Assessment (AMAP, 2021), referred to as *Eclipse* in this paper, and the CEDS emissions (Hoesly et al., 2018; Feng et al.,2020) combined with selected Shared Socio-economic Pathways (SSP) scenarios used in the CMIP6 future projections (Eyring et al., 2016), collectively referred to as *CMIP6* in this paper.

### 2.2.1. EclipseV6b emissions

The ECLIPSE V6b emissions dataset is a further evolution of the scenarios established in the EU funded ECLIPSE project (Stohl et al., 2015; Klimont et al., 2017). It has been developed with the global implementation of the GAINS (Greenhouse gas – Air pollution Interactions and Synergies) model (Amann et al., 2011). The GAINS model includes all key air pollutants and Kyoto greenhouse gases, where emissions are estimated for nearly 200 country-regions and several hundred source-sectors representing anthropogenic emissions. For this work, annual emissions were spatially distributed on $0.5°\times0.5°$ lon-lat grids for nine sectors: energy, industry, solvent use, transport, residential combustion, agriculture, open burning of agricultural waste, waste treatment, gas flaring and venting, and international shipping. A monthly pattern for each gridded layer was provided at a $0.5°\times0.5°$ grid level. The ECLIPSE V6b dataset, used in this study, includes an estimate for 1990 to 2015 using statistical data and two scenarios extending to 2050 that rely on the same energy projections from the World Energy Outlook 2018 (IEA, 2018) but have different assumptions about the implementation of air pollution reduction technologies, as described below.

The Current Legislation (CLE) scenario assumes efficient implementation of the current air pollution legislation committed before 2018, while the Maximum Feasible Reduction (MFR) scenario assumes implementation of best available emission reduction technologies included in the GAINS model. The MFR scenario demonstrates the additional reduction potential of $SO_2$ emissions by up to 60% and 40%, by 2030 for Arctic Council member and observer countries respectively, with implementation of best available technologies mostly in the energy and industrial sectors and to a smaller extent via measures in the residential sector. The Arctic Council member countries' maximum reduction potential could be fully realized by 2030 whereas in the observer countries additional reductions of 15% to 20% would remain to be achieved between 2030 and 2050. The assumptions and the details for the CLE

264 and MFR scenarios (as well as other scenarios developed within the ECLIPSE V6b family)
265 can be found in Höglund-Isaksson et al. (2020) and Klimont et al. (in preparation).

266 2.2.2. CMIP6 emissions

267 The CMIP6 emission datasets include a historical time series generated by the Community
268 Emissions Data System (CEDS) for anthropogenic emissions (Hoesly et al., 2018; Feng et al.,
269 2020), open biomass burning emissions (van Marle et al., 2010 ), and the future emission
270 scenarios driven by the assumptions embedded in the Shared Socioeconomic Pathways
271 (SSPs) and Representative Concentration Pathways (RCPs) (Riahi et al., 2017) that include
272 specific air pollution storylines (Rao et al., 2017 ). Gridded CMIP6 emissions are aggregated
273 to nine sectors: agriculture, energy, industrial, transportation, residential–commercial–other,
274 solvents, waste, international shipping, and aircraft. SSP data for future emissions from
275 integrated assessment models (IAMs) are first harmonized to a common 2015 base-year
276 value by the native model per region and sector. This harmonization process adjusts the
277 native model data to match the 2015 starting year values with a smooth transition forward in
278 time, generally converging to native model results (Gidden et al., 2018). The production of
279 the harmonized future emissions data is described in Gidden et al. (2019).
280
281 2.2.3. Implementation of the emissions in the GISS-E2.1

282 The Eclipse V6b and CEDS emissions on 0.5° × 0.5° spatial resolution are regridded to 2° ×
283 2.5° resolution in order to be used in the various GISS-E2.1 simulations. In the GISS-E2.1
284 Eclipse simulations, the non-methane volatile organic carbons (NMVOC) emissions are
285 chemically speciated assuming the SSP2-4.5 VOC composition profiles. In the Eclipse
286 simulations, biomass burning emissions are taken from the CMIP6 emissions, which have
287 been pre-processed to include the agricultural waste burning emissions from the EclipseV6b
288 dataset, while the rest of the biomass burning emissions are taken as the original CMIP6
289 biomass burning emissions. In addition to the biomass burning emissions, the aircraft
290 emissions are also taken from the CMIP6 database to be used in the Eclipse simulations. As
291 seen in Figure 1, the emissions are consistently higher in the CMIP6 compared to the Eclipse
292 emissions. The main differences in the two datasets are mainly over south-east Asia (not
293 shown) . The CMIP6 emissions are also consistently higher on a sectoral basis compared to
294 the Eclipse emissions. The figure shows that for air pollutant emissions, the CMIP6 SSP1-2.6
295 scenario and the Eclipse MFR scenario follow each other closely, while the Eclipse CLE
296 scenario is comparable with the CMIP6 SSP2-4.5 scenario for most pollutants; that is to some
297 extent owing to the fact that the $CO_2$ trajectory of the Eclipse CLE and the SSP2-4.5 are very
298 similar (not shown). A more detailed discussion of differences between historical Eclipse and
299 CMIP6 as well as CMIP6 scenarios are provided in Klimont et al. (in preparation).

300 2.3.    Simulations
301
302 In order to contribute to the AMAP Assessment report (AMAP, 2021), the GISS-E2.1 model
303 participated with AMIP-type simulations, which aim to assess the trends of Arctic air

pollution and climate change in the recent past, as well as with fully-coupled climate simulations. Five fully-coupled Earth system models (ESMs) simulated the future (2015-2050) changes of atmospheric composition and climate in the Arctic (>60°N), as well as over the globe. We have carried out two AMIP-type simulations, one with winds nudged to NCEP (standard AMIP-type simulation in AMAP) and one with freely varying winds, where both simulations used prescribed SSTs and sea-ice (Table 1). The nudging extents from the first model layer up to 10 hPa, which is the top of the NCEP input. In the fully-coupled simulations, we carried out two sets of simulations, each with three ensemble members, that used the CLE and MFR emission scenarios. Each simulation in these two sets of scenarios were initialized from a set of three fully-coupled ensemble recent past simulations (1990-2014) to ensure a smooth continuation from CMIP6 to Eclipse emissions.

In addition to the AMAP simulations, we have also conducted CMIP6-type simulations in order to compare the climate aerosol burdens and their impacts on radiative forcing and climate impacts with those from the AMAP simulations. We have used the SSP1-2.6, 2-4.5, 3-7.0, and 3-7.0-lowNTCF scenarios representing different levels of emission mitigations in the CMIP6 simulations. SSP1 and SSP3 define various combinations of high or low socio-economic challenges to climate change adaptation and mitigation, while SSP2 describes medium challenges of both kinds and is intended to represent a future in which development trends are not extreme in any of the dimensions, but rather follow middle-of-the-road pathways (Rao et al., 2017). SSP1-2.6 scenario aims to achieve a 2100 radiative forcing level of 2.6 W m$^{-2}$, keeping the temperature increase below 2 °C compared to the preindustrial levels. The SSP2-4.5 describes a "middle of the road" socio-economic family with a 4.5 W m$^{-2}$ radiative forcing level by 2100. The SSP3- 7.0 scenario is a medium-high reference scenario. SSP3-7.0-lowNTCF is a variant of the SSP3-7.0 scenario with reduced near-term climate forcer (NTCF) emissions. The SSP3-7.0 scenario has the highest methane and air pollution precursor emissions, while SSP3-7.0-lowNTCF investigates an alternative pathway for the Aerosols and Chemistry Model Intercomparison Project (AerChemMIP: Collins et al., 2017), exhibiting very low methane, aerosol, and tropospheric-ozone precursor emissions – approximately in line with SSP1-2.6. As seen in Table 1, we have conducted one transient fully-coupled simulation from 1850 to 2014, and a number of future scenarios.

We have employed prescribed global and annual mean greenhouse ($CO_2$ and $CH_4$) concentrations, where a linear increase in global mean temperature of 0.2 °C/decade from 2019 to 2050 was assumed, which are approximately in line with the simulated warming rates for the SSP2-4.5 scenario (AMAP, 2021).

2.4.    Observations

The GISS-E2.1 ensemble has been evaluated against surface observations of BC, organic aerosols (sum of OC and secondary organic aerosols (SOA), referred as OA in the rest of the paper) and $SO_4^{2-}$, ground-based and satellite-derived AOD at 550 nm, as well as surface and satellite observations of surface air temperature, precipitation, sea surface temperature, sea-ice extent, cloud fraction, and liquid and ice water content in 1995-2014 period. The surface

monitoring stations used to evaluate the simulated aerosol levels have been listed in Table S1 and S2 in the supplementary materials.

*2.4.1. Aerosols*

Measurements of speciated particulate matter (PM), BC, $SO_4^{2-}$, and (OA) come from three major networks: the Interagency Monitoring of Protected Visual Environments (IMPROVE) for Alaska (The IMPROVE measurements that are in the Arctic (>60°N) are all in Alaska); the European Monitoring and Evaluation Programme (EMEP) for Europe; and the Canadian Air Baseline Measurements (CABM) for Canada (Table S1 and S2). In addition to these monitoring networks, BC, OA, and $SO_4^{2-}$ measurements from individual Arctic stations were used in this study. The individual Arctic stations are Fairbanks and Utqiagvik, Alaska (part of IMPROVE, though their measurements were obtained from their PIs); Gruvebadet and Zeppelin mountain (Ny Alesund), Norway; Villum Research Station, Greenland; and Alert, Nunavut (the latter being an observatory in Global Atmospheric Watch-WMO, and a part of CABM). The measurement techniques are briefly described in the supplement.

AOD at 500 nm from the AErosol RObotic NETwork (AERONET, Holben et al., 1998) was interpolated to 550 nm AOD using the Ångström formula (Ångström, 1929). We also used a new merged AOD product developed by Sogacheva et al. (2020) using AOD from 10 different satellite-based products. According to Sogacheva et al. (2020), this merged product could provide a better representation of temporal and spatial distribution of AOD. However, it is important to note that the monthly aggregates of observations for both AERONET and the satellite products depend on availability of data and are not likely to be the true aggregate of observations for a whole month when only few data points exist during the course of a month. In addition, many polar orbiting satellites take one observation during any given day, and typically at the same local time. Nevertheless, these data sets are key observations currently available for evaluating model performances. Information about the uncertain nature of AOD observations can be found in previous studies (e.g. Sayer et al., 2018; Sayer and Knobelspiesse, 2019; Wei et al., 2019; Schutgens et al., 2020, Schutgens, 2020; Sogacheva et al., 2020).

*2.4.2. Surface air temperature, precipitation, and sea-ice*

Surface air temperature and precipitation observations used in this study are from University of Delaware gridded monthly mean data sets (UDel; Willmott and Matsuura, 2001). UDel's 0.5° resolution gridded data sets are based on interpolations from station-based measurements obtained from various sources including the Global Historical Climate Network, the archive of Legates and Willmott and others.  The Met Office Hadley Center's sea ice and sea surface temperature (HadISST; Rayner et al., 2003) was used for evaluating model simulations of sea ice and SSTs. HadISST data is an improved version of its predecessor known as global sea ice and sea surface temperature (GISST). HadISST data is constructed using information from a variety of data sources such as the Met Office Marine Database, Comprehensive Ocean-Atmosphere Data Set, passive microwave remote sensing retrieval and sea ice charts.

*2.4.3. Satellite observations used for cloud fraction  and cloud liquid water and ice water*

The Advanced Very High Resolution Radiometer (AVHRR-2) sensors onboard the NOAA and EUMETSAT polar orbiting satellites have been flying since the early 1980s. These data have been instrumental in providing the scientific community with climate data records spanning nearly four decades. Tremendous progress has been made in recent decades in improving, training and evaluating the cloud property retrievals from these AVHRR sensors. In this study, we use the retrievals of total cloud fraction from the second edition of EUMETSATs Climate Monitoring Satellite Application Facility (CM SAF) Cloud, Albedo and surface Radiation data set from AVHRR data (CLARA-A2, Karlsson et al., 2017). This cloud property climate data record is available for the period 1982-2018. Its strengths and weaknesses and inter-comparison with the other similar climate data records are documented in Karlsson and Devasthale (2018). Further data set documentation including Algorithm Theoretical Basis and Validation reports can be found in Karlsson et al. (2017).

Cloud liquid and ice water path estimates derived from the cloud profiling radar on board CloudSat (Stephens et al., 2002) and constrained with another sensor onboard NASA's A-Train constellation, MODIS-Aqua (Platnick et al., 2015), are used for the model evaluation. These Level 2b retrievals, available through 2B-CWC-RVOD product (Version 5), for the period 2007-2016 are analysed. This constrained version is used instead of its radar-only counterpart, as it uses additional information about visible cloud optical depths from MODIS, leading to better estimates of cloud liquid water paths. Because of this constraint the data are available only for the day-lit conditions, and hence, are missing over the polar regions during the respective winter seasons. The theoretical basis for these retrievals can be found in http://www.cloudsat.cira.colostate.edu/sites/default/files/products/files/2B-CWC-RVOD_PDICD.P1_R05.rev0_.pdf (last access: October 26th 2020). Being an active cloud radar, CloudSat provides orbital curtains with a swath width of just about 1.4 km. Therefore, the data are gridded at 5°x5° to avoid too many gaps or patchiness and to provide robust statistics.

## 3.      Results

### 3.1.      Evaluation

The simulations are compared against surface measurements of BC, OA, $SO_4^{2-}$ and AOD, as well as surface and satellite measurements of surface air temperature, precipitation, sea surface temperature, sea-ice extent, total cloud fraction, liquid water path, and ice water path described in section 2.4, by calculating the correlation coefficient (*r*) and normalized mean bias (*NMB*). OA refers to the sum of primary organic carbon (OC) and secondary organic aerosols (SOA).

*3.1.1.  Aerosols*

The recent past simulations are for BC, OA, SO4 and AOD (Table 2) against available surface measurements. The monthly observed and simulated time series for each station are accumulated per species in order to get a full Arctic timeseries data, which also includes spatial variation, to be used for the evaluation of the model. In addition to Table 2, the climatological mean (1995-2014) of the observed and simulated monthly surface concentrations of BC, OA, $SO_4^{2-}$ and AOD at 550 nm (note that AOD is averaged over 2008, 2009 and 2014) are shown in Figure 2. The AOD observation data for years 2008, 2009, and 2014 are used in order to keep the comparisons in line with the multi-model evaluations being carried out in the AMAP assessment report (AMAP, 2021). We also provide spatial distributions of the NMB, calculated as the mean of all simulations for BC, OA, SO4 and AOD in Figure 3. The statistics for the individual stations are provided in the Supplementary Material, Tables S3-S6.

Results showed overall an underestimation of aerosol species over the Arctic, as discussed below. Surface BC levels are underestimated at all Arctic stations from 15% to 90%. Surface OA levels are also underestimated from -5% to -70%, except for a slight overestimation of <1% over Karvatn (B5) and a large overestimation of 90% over Trapper Creek (B6). Surface $SO_4^{2-}$ concentrations are also consistently underestimated from -10% to -70%, except for Villum Research Station (S11) over northeastern Greenland where there is an overestimation of 45%. Finally, AODs are also underestimated over all stations from 20% to 60%. Such underestimations at high latitudes have also been reported by many previous studies (e.g. Skeike et al., 2011; Eckhardt et al., 2015; Lund et al., 2017, 2018; Schacht et al., 2019; Turnock et al., 2020), pointing to a variety of reasons including uncertainties in emission inventories, errors in the wet and dry deposition schemes, the absence or underrepresentation of new aerosol formation processes, and the coarse resolution of global models leading to errors in emissions and simulated meteorology, as well as in representation of point observations in coarse model grid cells. Turnock et al. (2020) evaluated the air pollutant concentrations in the CMIP6 models, including the GISS-E2.1 ESM, and found that observed surface $PM_{2.5}$ concentrations are consistently underestimated in CMIP6 models by up to 10 $\mu g\ m^{-3}$, particularly for the Northern Hemisphere winter months, with the largest model diversity near natural emission source regions and the Polar regions.

The BC levels are largely underestimated in simulations by 50% (CMIP6_Cpl_Hist) to 67% (Eclipse_AMIP). The CMIP6 simulations have lower bias compared to EclipseV6b simulations due to higher emissions in the CMIP6 emission inventory (Figure 1). Within the EclipseV6b simulations, the lowest bias (-57%) is calculated for the Eclipse_AMIP_NCEP simulation, while the free climate and coupled simulations showed a larger underestimation (>62%), which can be attributed to a better simulation of transport to the Arctic when nudged winds are used. The Eclipse simulations also show that the coupled simulations had slightly smaller biases (*NMB*=-63%) compared to the AMIP-type free climate simulation (AMIP-OnlyAtm: *NMB*=-67%). The climatological monthly variation of the observed levels is poorly reproduced by the model with *r* values around 0.3. BC levels are mainly underestimated in winter and spring, which can be attributed to the underestimation of the

478    anthropogenic emissions of BC, while the summer levels are well captured by the majority of
479    the simulations (Figure 2).
480
481    Surface OA concentrations are underestimated from 8% (Eclipse_AMIP_NCEP) to 35%
482    (Eclipse_AMIP) by the Eclipse ensemble, while the CMIP6_Cpl_Hist simulation
483    overestimated surface OA by 13%. The Eclipse simulations suggest that the nudged winds
484    lead to a better representation of transport to the Arctic, while the coupled simulations had
485    smaller biases compared to the AMIP-type free climate simulation (AMIP-OnlyAtm), similar
486    to BC. The climatological monthly variation of the observed concentrations are reasonably
487    simulated, with $r$ values between 0.51 and 0.69 (Table 2 and Figure 2). As can be seen in
488    Figure S1, the OA levels are dominated by the biogenic SOA, in particular via α-pinene
489    (monoterpenes) oxidation, compared to anthropogenic (by a factor of 4-9) and biomass
490    burning (by a factor of 2-3) OA. While OC and BC are emitted almost from similar sources,
491    this biogenic-dominated OA seasonality also explains why simulated BC seasonality is not as
492    well captured, suggesting the underestimations in the anthropogenic emissions of these
493    species, in particular during the winter. It should also be noted that GISS-E2.1 does not
494    include marine VOC emissions except for DMS, while these missing VOCs such as isoprene
495    and monoterpenes are suggested to be important sources for the summer time aerosol levels
496    over the Arctic (Ornella et al., 2011; Karl et al., 2013; Schmale et al., 2021).
497
498    Surface $SO_4^{2-}$ levels are simulated with a smaller bias compared to the BC levels, however
499    still underestimated by 40% (CMIP6_Cpl_Hist) to 53% (Eclipse_AMIP_NCEP). The
500    Eclipse_AMIP_NCEP simulation is biased higher (NMB=-53%) compared to the
501    Eclipse_AMIP (NMB=-50%), probably due to higher cloud fraction simulated by the nudged
502    version (see section 3.1.6), leading to higher in-cloud $SO_4^{2-}$ production. The climatological
503    monthly variation of observed $SO_4^{2-}$ concentrations are reasonably simulated in all
504    simulations (r=0.65-0.74). The observed springtime maximum is well captured by the GISS-
505    E2.1 ensemble, with underestimations in all seasons, mainly suggesting underestimations in
506    anthropogenic $SO_2$ emissions (Figure 2), as well as simulated cloud fractions, which have
507    high positive bias in winter and transition seasons, while in summer, the cloud fraction is well
508    captured with a slight underestimation. The clear sky AOD over the Aeronet stations in the
509    Arctic region is underestimated by 33% (Eclipse_AMIP) to 47% (Eclipse_CplHist1). Similar
510    negative biases are found with comparison to the satellite based AOD product (Table 2). The
511    climatological monthly variation is poorly captured with $r$ values between -0.07 to 0.07
512    compared to AERONET AOD and 0 to 0.13 compared to satellite AOD. The simulations
513    could not represent the climatological monthly variation of the observed AERONET AODs
514    (Figure 2).
515
516    *3.1.2. Climate*
517    The different simulations are evaluated against a set of climate variables and the statistics are
518    presented in Table 3a and 3b, and in Figures 4 and 5. The climatological mean (1995-2014)
519    monthly  Arctic surface air temperatures are slightly overestimated by up to 0.55 °C in the
520    AMIP simulations, while the coupled ocean simulations underestimate the surface air
521    temperatures by up to -0.17 °C. All simulations were able to reproduce the monthly

climatological variation with $r$ values of 0.99 and higher (Figure 4). Results show that both absorbing (BC) and scattering aerosols (OC and $SO_4^{2-}$) are underestimated by the GISS-E2.1 model, implying that these biases can partly cancel out their impacts on radiative forcing due to aerosol-radiation interactions. This, together with the very low biases in surface temperatures suggests that the effects of the anthropogenic aerosols on the Arctic climate via radiation is not the main driver in comparison to cloud indirect effects and forcing from greenhouse gases. The monthly mean precipitation has been underestimated by around 50% by all simulations (Table 3a), with largest biases during the summer and autumn (Figure 4). The observed monthly climatological mean variation was very well simulated by all simulations, with $r$ values between 0.80 and 0.90.

Arctic SSTs are underestimated by the ocean-coupled simulation up to -1.96 °C, while the atmosphere-only runs underestimated SSTs by -1.5 °C (Table 3a). The negative bias in atmosphere-only simulations is due to the different datasets used to drive the model, which a combined product of HadISST and NOAA-OI2 (Reynolds et al., 2002) and to evaluate the model (Rayner et al., 2003), which is only HadISST. The monthly climatological mean variation is well captured with $r$ values above 0.99 (Table 3a, Figure 4), with a similar cold bias in almost all seasons. The sea-ice extent was overestimated by all coupled simulations by about 12%, while the AMIP-type Eclipse simulations slightly underestimated the extent by 3% (Table 3a). The observed variation was also very well captured with very high $r$ values. The winter and spring biases were slightly higher compared to the summer and autumn biases (Figure 4).

All simulations overestimate the climatological (1995-2014) mean total cloud fraction by 21% to 25% during the extended winter months (October through February), where the simulated seasonality is anti-correlated in comparison to AVHRR CLARA-A2 observations, whereas, a good correlation is seen during the summer months irrespective of the observational data reference. The largest biases were simulated by the atmosphere-only simulations, with the nudged simulation having the largest bias ($NMB$=25%). The coupled model simulations are closer to the observations during the recent past. On the other hand, the climatology of the annual-mean cloud fraction was best simulated by the nudged atmosphere-only simulation (Eclipse_AMIP_NCEP) with a $r$ value of 0.40, while other simulations showed a poor performance ($r$=-0.17 to +0.10), except for the summer where the bias is lowest (Figure 5). The evaluation against CALIPSO data however shows much smaller biases ($NMB$ = +3% to +6%). This is because in comparison to CALIPSO satellite that carries an active lidar instrument (CALIOP), the CLARA-A2 dataset has difficulties in separating cold and bright ice/snow surfaces from clouds thereby underestimating the cloudiness during Arctic winters. Here both datasets are used for the evaluation as they provide different observational perspectives and cover the typical range of uncertainty expected from the satellite observations. Furthermore, while the CLARA-A2 covers the entire evaluation period in current climate scenario, CALIPSO observations are based on 10-year data covering the 2007-2016 period.

565    Figure 5 shows the evaluation of the simulations with respect to LWP and IWP. It has to be
566    noted here that to obtain a better estimate of the cloud water content, the CloudSat
567    observations were constrained with MODIS observations which resulted in a lack of data
568    during the months with darkness (Oct-Mar) over the Arctic (see Section 2.4.3). Hence, we
569    present the results for the polar summer months only. As seen in Figure 5, all simulations
570    overestimated the climatological (2007-2014) mean Polar summer LWP by up to almost
571    75%. The smallest bias (14%) is calculated for the nudged atmosphere-only
572    (Eclipse_OnlyAtm_NCEP), while the coupled simulations had biases of 70% or more.
573    Observations show a gradual increase in the LWP, peaking in July, whereas the model
574    simulates a more constant amount for the nudged simulation and a slightly decreasing
575    tendency for the other configurations. All model simulations overestimate LWP during the
576    spring months. The atmosphere-only nudged simulations tend to better simulate the observed
577    LWP during the summer months (June through September). The coupled simulations,
578    irrespective of the emission dataset used, are closer to observations only during the months of
579    July and August.
580
581    The climatological (2007-2014) mean Polar summer IWP is slightly better simulated
582    compared to the LWP, with biases within -60% with the exception of the nudged Eclipse
583    (Eclipse_AMIP_NCEP) simulation (*NMB*=-74%). All simulations simulated the monthly
584    variation well, with *r* values of 0.95 and more. In the Arctic, the net cloud forcing at the
585    surface changes sign from positive to negative during the polar summer (Kay and L'Ecuyer,
586    2013). This change typically occurs in May driven mainly by shortwave cooling at the
587    surface. Since the model simulates the magnitude of the LWP reasonably, particularly in
588    summer, the negative cloud forcing can also be expected to be realistic in the model (e.g.
589    Gryspeerdt et al. 2019). Furthermore, the aerosol and pollution transport into the Arctic
590    typically occurs in the lowermost troposphere where liquid water clouds are prevalent during
591    late spring and summer seasons (Stohl, 2006; Law et al., 2014; Thomas et al., 2019). The
592    interaction of ice clouds with aerosols is, however, more complex, as ice clouds could have
593    varying optical thicknesses, with mainly thin cirrus in the upper troposphere and relatively
594    thicker clouds in the layers below. Without the knowledge on the vertical distribution of
595    optical thickness, it is difficult to infer the potential impact of the underestimation of IWP on
596    total cloud forcing and their implications.
597
598    3.2. Arctic burdens and radiative forcing due to aerosol-radiation interactions (RF$_{ARI}$)
599
600    The recent past and future Arctic column burdens for BC, OA and SO$_4^{2-}$ for the different
601    scenarios and emissions are provided in Figure 6. In addition, Table 4 shows the calculated
602    trends in the burdens for BC, OA and SO$_4^{2-}$ for the different scenarios, while Table 5
603    provides the 1990-2010 and 2030-2050 mean burdens of the aerosol components. The BC
604    and SO$_4^{2-}$ burdens started decreasing from the 1990s, while OA burden remains relatively
605    constant, although there is large year-to-year variability in all simulations. All figures show a
606    decrease in burdens after 2015, except for the SSP3-7.0 scenario, where the burdens remain
607    close to the 2015 levels. The high variability in BC and OA burdens over the 2000's is due to
608    the biomass burning emissions from GFED, which have not been harmonized with the no-

609  satellite era. It should also be noted that these burdens can be underestimated considering the
610  negative biases calculated for the surface concentrations and in particular for the AODs
611  reported in Table 2 and Tables S2-6.
612
613  In addition to the burdens of these aerosol species, the TOA radiative forcing due to aerosol-
614  radiation interaction ($RF_{ARI}$) over the Arctic are simulated by the GISS-E2.1 ensemble. $RF_{ARI}$
615  is calculated  as the sum of shortwave and longwave forcing from the individual aerosol
616  species between 1850 and 2050 are presented in Figure 7. It is important to note that the
617  present study uses the instantaneous forcing diagnostics from the model, which are calculated
618  with a double call to the model's radiation code, with and without aerosols, as described in
619  Bauer et al. (2020) and Miller et al. (2021), and not the effective radiative forcing. The
620  transient cloud radiative effect in GISS-E.2.1 follows Ghan (2013), which calculates the
621  difference in cloud radiative forcing with aerosol scattering and absorption omitted (Bauer et
622  al., 2020). However, the present study only focuses on the $RF_{ARI}$. The model outputs separate
623  forcing diagnostics for anthropogenic and biomass burning BC and OC, as well as biogenic
624  SOA, making it possible to attribute the forcing to individual aerosol species. The negative
625  $RF_{ARI}$ has increased significantly since 1850 until the 1970's due to an increase in aerosol
626  concentrations. Due to the efforts of mitigating air pollution and thus a decrease in emissions,
627  the forcing became less negative after the 1970's until 2015. Figure 7 also shows a visible
628  difference in the anthropogenic $RF_{ARI}$ simulated by the NINT (prescribed aerosols) and OMA
629  (interactive aerosols) simulations in the CMIP6 ensemble, where the anthropogenic $RF_{ARI}$ by
630  NINT simulation is less negative (by almost 30%) compared to the OMA simulation (Figure
631  7b). On the other hand, no such difference is seen in the net $RF_{ARI}$ time series (Figure 7a).
632  This compensation is largely driven by the 50% more positive dust and 10% less negative
633  sea-salt $RF_{ARI}$ in the OMA simulation.
634
635  *3.2.1. Black carbon*
636  All simulations show a statistically significant (as calculated by Mann-Kendall trend
637  analyses) decrease in the Arctic BC burdens (Table 4) between 1990-2014, except for the
638  CMIP6_Cpl_Hist, which shows a slight non-significant increase that can be attributed to the
639  large increase in global anthropogenic BC emissions in CMIP6 after year 2000 (Figure 1).
640  From 2015 onwards, all future simulations show a statistically significant decrease in the
641  Arctic BC burden (Table 4).  The Eclipse CLE ensemble shows a 1.1 kTon (31%) decrease in
642  the 2030-2050 mean Arctic BC burden compared to the 1990-2010 mean, while the decrease
643  in 2030-2050 mean Arctic BC burden is larger in the MFR ensemble (2.3 kTon: 62%). In the
644  CMIP6 simulations, the  2030-2050 mean Arctic BC burdens decrease by 0.70 to 1.59 kTon,
645  being largest in SSP1-2.6 and lowest in SSP3-7.0-lowNTCF, while the SSP3-7.0 simulation
646  leads to an increase of 0.43 kTon (12%) in 2030-2050 mean Arctic BC burdens. It is
647  important to note that the changes in burden simulated by the Eclipse CLE ensemble (-1.1
648  kTon) is comparable with the change of -1 kTon in the SSP2-4.5 scenario, consistent with the
649  projected emission changes in the two scenarios (Figure 1).
650
651  As seen in Table 6, the GISS-E2.1 ensemble calculated a BC $RF_{ARI}$ of up to 0.23 W m$^{-2}$ over
652  the Arctic, with both CMIP6 and Eclipse coupled simulations estimating the highest forcing

653 of 0.23 W m$^{-2}$ for the 1990-2010 mean (Table 6a). This agrees with previous estimates of the
654 BC RF$_{ARI}$ over the Arctic (e.g. Schacht et al., 2019). In the future, the positive BC RF$_{ARI}$ is
655 generally decreasing (Figure 6) due to lower BC emissions and therefore burdens, except for
656 the SSP3-7.0 scenario, where the BC forcing becomes more positive by 0.05 W m$^{-2}$ due to
657 increasing BC emissions and burdens The changes in the Arctic RF$_{ARI}$ in Table 6a follows
658 the Arctic burdens presented in Table 5, and emission projections presented in Figure 1,
659 leading to largest reductions in BC RF$_{ARI}$ simulated in SSP1-2.6 (-0.10 Wm$^{-2}$). Similar to the
660 burdens, the Eclipse CLE and CMIP6 SSP2-4.5 scenarios simulate a very close decrease in
661 the 2030-2050 mean BC RF$_{ARI}$ of -0.06 Wm$^{-2}$ and -0.06 Wm$^{-2}$, respectively.
662
663 *3.2.2. Organic aerosols*
664 The Eclipse historical ensemble simulate a positive OA burden trend between 1990 and 2014,
665 however this trend is not significant at the 95% confidence level (Table 4). The
666 CMIP6_Cpl_Hist simulation gives a larger trend, due to a large increase in global
667 anthropogenic OC emissions in CMIP6 (Figure 1). The nudged AMIP Eclipse simulation
668 calculates the largest 1990-2010 mean OA burden (57 kTon), while the coupled simulation
669 shows a slightly lower 1990-2010 mean burden (55 kTon). This largest OA burden in the
670 Eclipse_AMIP_NCEP simulation is attributed to the largest biogenic SOA burden calculated
671 in this scenario, as well as a better-simulated transport from source regions due to the nudged
672 winds (Figure S1). The anthropogenic and biogenic contributions to SOA burdens in the
673 coupled Eclipse and CMIP6 recent past simulations imply that the differences in the burdens
674 between the two ensembles can be attributed to the different anthropogenic emissions
675 datasets used in the Eclipse and CMIP6 simulations (Figure S1), as well as the differences in
676 SOA contributions due to simulated increases in the biogenic emissions (Figure S5) . The
677 AMIP-type Eclipse run simulates a lower 1990-2010 mean OA burden (50 kTon), attributed
678 to the smallest biogenic SOA burden in this scenario. The Eclipse CLE ensemble shows a
679 decrease of 6.6 kTon (12%) in 2030-2050 mean OA burden compared to the 1990-2010
680 mean, while the MFR ensemble shows a larger decrease in the same period (15.2 kTon:
681 27%). The CMIP6 simulations show a much larger decrease of 2030-2050 mean Arctic OA
682 burdens, with a decrease of 8.1 kTon (SSP2-4.5) to 17 kTon (SSP1-2.6), while the SSP3-7.0
683 simulation shows an increase in OA burdens in the same period by 1.3 kTon (2%). Similar to
684 BC burdens, Eclipse CLE and CMIP6 SSP2-4.5 scenarios project similar changes in 2030-
685 2050 mean OA burden (6.6 kTon and 8.1 kTon, respectively).
686
687 As shown in Table 6a, the Eclipse ensemble calculated an OA RF$_{ARI}$ of -0.05 to -0.08 Wm$^{-2}$
688 for the 1990-2010 mean, where the nudged AMIP-type simulation shows the largest RF$_{ARI}$,
689 due to the largest Arctic OA burden calculated for this period (Table 5). For the future, both
690 Eclipse CLE and MFR ensembles show an increase in the negative 2030-2050 mean RF$_{ARI}$
691 by -0.02 Wm$^{-2}$, which is very close to the increase in the negative forcing calculated for the
692 various CMIP6 simulations (-0.01 to -0.03 Wm$^{-2}$). Following the burdens, the largest increase
693 in the 2030-2050 mean OA RF$_{ARI}$ is calculated for the SSP3-7.0 (-0.03 Wm$^{-2}$), and the lowest
694 for SSP1-2.6 and 3-7.0-lowNTCF (-0.01 Wm$^{-2}$).
695
696 *3.2.3. Sulfate*

697 Regarding $SO_4^{2-}$ burdens, all simulations show a statistically significant negative trend both
698 in 1990-2014 and in 2015-2050, as seen in Figure 6 and Table 5. Both the nudged AMIP-type
699 and coupled Eclipse simulations showed a 1990-2010 mean $SO_4^{2-}$ burden of 93 kTon, while
700 the AMIP-type simulation showed a slightly larger $SO_4^{2-}$ burden of 95 kTon, attributed to the
701 larger cloud fraction simulated in this model version (Table 2). For the 2015-2050 period, the
702 Eclipse ensemble simulates a mean Arctic $SO_4^{2-}$ burden decrease of 30-40 kTon (32-42%),
703 compared to the 1990-2010 mean, while CMIP6 ensemble simulates a reduction of 16-45
704 kTon (16-45%). The SSP2-4.5 and Eclipse CLE scenarios simulate a very similar decrease
705 (30 kTon) in 2030-2050 mean Arctic $SO_4^{2-}$ burdens, while the MFR and SSP1-2.6 scenarios
706 also simulate comparable reductions in the burdens (Table 5). Following the emission
707 projections, the SSP1-2.6 scenario gives the largest decrease (45 kTon: 45%), and the SSP3-
708 7.0 scenario gives the smallest reduction (16 kTons: 16%) in Arctic 2030-2050 mean $SO_4^{2-}$
709 burdens.
710
711 The $SO_4^{2-}$ $RF_{ARI}$ is decreasing (Figure 6) following the decreasing emissions (Figure 1) and
712 burdens (Figure 5). Both Eclipse and CMIP6 ensembles simulate a decrease in $SO_4^{2-}$ $RF_{ARI}$
713 by 0.06-0.18 $Wm^{-2}$. The 2030-2050 mean $SO_4^{2-}$ $RF_{ARI}$ follows the burdens (Table 6), with
714 CLE and SSP2-4.5 giving similar decreases in the negative $SO_4^{2-}$ $RF_{ARI}$ of 0.11 $Wm^{2-}$, while
715 the Eclipse MFR and SSP1-2.6 simulates a very similar decrease in the 2030-2050 mean
716 $SO_4^{2-}$ $RF_{ARI}$ (0.16 and 0.18 $Wm^{-2}$, respectively).
717
718 *3.2.4. Net aerosol radiative forcing*
719 The coupled simulations in both Eclipse and CMIP6 ensemble show an Arctic $RF_{ARI}$ of -0.32
720 to -0.35 $Wm^{-2}$ for the 1990-2010 mean, slightly lower than recent estimates (e.g. -0.4 $W\ m^{-2}$
721 by Markowicz et al., 2021). In the Eclipse ensemble, -0.22±0.01 $Wm^{-2}$ is calculated to be
722 originated by the anthropogenic aerosols, while in the CMIP6 near-past simulations show a
723 contribution of -019 to -0.26 $Wm^{-2}$ from anthropogenic aerosols (Table 6b). The AMIP-type
724 Eclipse simulations calculated a much larger $RF_{ARI}$ of -0.47 $W\ m^{-2}$ for the same period,
725 which can be mainly due to the increase in the positive forcing of the BC aerosols in the
726 coupled simulations due to larger burdens. This effect is amplified due to the larger sea-ice
727 concentration simulated with the coupled model, leading to brighter surfaces compared to the
728 AMIP simulations. For the 2030-2050 period, the Eclipse ensemble simulated an increase in
729 the negative in $RF_{ARI}$ by -0.07 $W\ m^{-2}$, while the negative anthropogenic in $RF_{ARI}$ increased
730 by only -0.02 $W\ m^{-2}$, suggesting that the contribution from natural aerosols become more
731 important in the future. The results show that the positive dust forcing is decreased by 0.03
732 $Wm^{-2}$ (from 0.12 $Wm^{-2}$ to 0.09 $Wm^{-2}$), while the negative sea-salt forcing becomes more
733 negative by -0.03 $Wm^{-2}$ due to the increase of ice-free ocean fraction due to melting of sea-
734 ice (see Section 3.3). For the same period, the CMIP6 future ensemble simulated an increase
735 of the negative $RF_{ARI}$ by -0.01 $Wm^{-2}$ to -0.06 $Wm^{-2}$, the largest change being in SSP1-2.6 and
736 SSP2-4.5, mainly driven by the change in BC forcing (Table 6a). Table 6 also shows that the
737 SSP1-1.6 simulates no change in the anthropogenic forcing, while SSP2-4.5 shows a similar
738 increase of -0.01 $Wm^{-2}$ in the Eclipse ensemble. In contrary, the SSP3-7.0 and SSP3-7.0-
739 lowNTCF simulates a large decrease in the anthropogenic negative $RF_{ARI}$ by 0.05 $Wm^{-2}$ and
740 0.02 $Wm^{-2}$, respectively.

741

742 The different behavior in the two ensembles is further investigated by looking at the aerosol-
743 radiation forcing calculated for the individual aerosol species of BC, OA, $SO_4^{2-}$ and $NO_3^-$
744 presented in Figure 8 that shows the box-whisker plots using the similar scenarios in the
745 Eclipse (CLE and MFR) and CMIP6 (SSP2-4.5 and SSP1-2.6) ensembles. The increase in
746 cooling effect of aerosols calculated by the Eclipse ensemble is attributed mainly to the
747 decrease in BC as opposed to other aerosol species (Figure 8). More negative forcing is
748 calculated for the OA and $NO_3^-$, while the $SO_4^{2-}$ forcing is becoming less negative due to
749 large reductions in $SO_2$ emissions (Figure 1). The net aerosol forcing is therefore slightly
750 more negative. In the CMIP6 ensemble, the BC forcing does not change as much compared
751 to the Eclipse ensemble to counteract the change in impact from $SO_4^{2-}$, giving a more
752 negative net aerosol forcing, slightly smaller compared to the Eclipse ensemble. The CMIP6
753 ensemble also simulates a larger increase in the negative $NO_3^-$ forcing compared to the
754 Eclipse ensemble (Shindell et al., 2013). Overall, the changes in the different aerosol species
755 leads to a more negative aerosol forcing by mid-century (2030-2050) compared to the 1990-
756 2010 period.

757

758 The spatial distributions of the statistically significant change in the Arctic $RF_{ARI}$ in 2030-
759 2050 mean with respect to the 1990-2010 mean in the different ensemble members are
760 presented in Figure 9. Results show a decrease of the negative $RF_{ARI}$ over Europe, and partly
761 over North America, and an increase over northern Pacific in all ensemble members.
762 Globally, larger changes are simulated over the East and South Asia (Figure S2), where
763 largest anthropogenic emission reductions take place. The global net $RF_{ARI}$ is dominated by
764 the sea-salt particles, accounting for about 60% of the 1990-2010 mean forcing of -2 to -2.3
765 $Wm^{-2}$ in and 2030-2050 mean forcing of -19 to 2.1 $Wm^{-2}$.

766

767 3.3. Climate change

768

769 *3.3.1. Surface air and sea surface temperatures*
770 The surface air temperature and sea-ice extent are calculated in the different simulations for
771 the 1990-2050 period. As seen in Figure 10, the Arctic surface air temperatures increase in all
772 scenarios. Between 1990 and 2014, the surface air temperatures over the Arctic increased
773 statistically significant by 0.5 °C decade$^{-1}$ (Eclipse_CplHist) to 1 °C decade$^{-1}$
774 (CMIP6_Cpl_Hist), with CMIP6 showing larger increases compared to the Eclipse ensemble
775 (Table 7) . On the other hand, the observed surface air temperature during 1990-2014 shows a
776 smaller and statistically non-significant increase of 0.2 °C decade$^{-1}$. From 2015 onwards,
777 surface air temperatures continue to increase significantly by 0.3 to 0.6 °C decade$^{-1}$, with
778 larger increases in the Eclipse ensemble, due to larger reductions in the emissions and
779 therefore in the burdens and associated $RF_{ARI}$.

780

781 The 2030-2050 mean surface air temperatures are projected to increase by 2.1 °C and 2.3 °C
782 compared to the 1990-2010 mean temperature (Table 8, Figure 10) according to the Eclipse
783 CLE and MFR ensembles, respectively, while the CMIP6 simulation calculated an increase
784 of 1.9 °C (SSP1-2.6) to 2.2 °C (SSP3-7.0). Changes in both ensembles are statistically

785   significant on a 95% level. These warmings are smaller compared to the 4.5 - 5 °C warmer
786   2040 temperatures compared to the 1950-1980 average in the CMIP6 SSP1-2.6, SSP2-4.5
787   and SSP3-7.0 scenarios, reported by Davy and Outen (2020). It should however be noted that
788   due to the different baselines used in the present study (1990-2010) and the 1950-1980
789   baseline used in Davy and Outen (2020), it is not possible to directly compare these datasets.
790   Figure 11 shows the spatial distributions of the statistically significant (as calculated by
791   student t-test) Arctic surface air temperature change between the 1990-2010 mean and the
792   2030-2050 mean for the individual Eclipse and CMIP6 future scenarios. All scenarios
793   calculate a warming in the surface air temperatures over the central Arctic, while there are
794   differences over the land areas. The Eclipse CLE and MFR ensembles show similar warming
795   mainly over the Arctic ocean as well as North America and North East Asia and cooling over
796   the Greenland Sea. The latter is a well-known feature of observations and future projections,
797   linked, i.e., to the deep mixed layer in the area and declines in the Atlantic Meridional
798   Circulation (e.g. IPCC, 2014; Menary and Wood, 2018; Keil et al., 2020). There are also
799   differences between the Eclipse and the CMIP6 ensembles as seen in Figure 11. All CMIP6
800   scenarios show a warming over the central Arctic and a limited cooling over northern
801   Scandinavia, following the changes in $RF_{ARI}$ shown in Figure 9, except for the SSP3-7.0
802   scenario that shows no cooling in the region. The SSP3-7.0-lowNTCF scenario shows an
803   additional cooling over Siberia. These warmings are comparable with earlier studies, such as
804   Samset et al. (2017) estimating a warming of 2.8 °C, attributed to aerosols.
805
806   *3.3.2. Sea-ice*
807   The Arctic sea-ice extent is found to decrease significantly in all simulations (Figure 10 and
808   Table 7). Similar to the near-surface temperatures, during the 1990-2014 period, the CMIP6
809   ensemble simulated a large decrease of sea-ice extent compared to the Eclipse ensemble. On
810   the other hand, the CMIP6_Cpl_Hist largely overestimated the observed decrease of 30 000
811   $km^2 yr^{-1}$. This overestimation has also been reported for some of the CMIP5 and CMIP6
812   models (Davy and Outten, 2020). After 2015, the Eclipse CLE ensemble projected larger
813   decreases in the sea-ice extent compared to the CMIP6 ensemble (Table 7), in agreement
814   with the changes in the near-surface temperatures. The evolutions of March and September
815   sea-ice extents, representing the Arctic annual maximum and minimum extents, respectively,
816   are also analyzed. The Eclipse ensemble projects a decrease of $23\,000 \pm 11\,000$ $km^2 yr^{-1}$ in
817   March sea-ice extent during the 2015-2050 period, while the CMIP6 ensemble projects a
818   decrease of $10\,000 \pm 6000$ $km^2 yr^{-1}$ for the same period, both statistically significant. In
819   September, much larger decreases are projected by both ensembles. The Eclipse ensemble
820   simulates a decrease of $64\,000 \pm 10\,000$ $km^2 yr^{-1}$ in the 2015-2050 period while the CMIP6
821   ensemble predicts a decrease of $50\,000 \pm 20\,000$ $km^2 yr^{-1}$.
822
823   The 2030-2050 annual mean sea-ice extent (Table 8) is projected to be 1.5 and 1.7 million
824   $km^2$ lower compared to the 1990-2010 mean in the Eclipse CLE and MFR scenarios,
825   respectively, both statistically significant on a 95% level. The CMIP6 simulations predict a
826   lower decrease of sea-ice extent by 1.2 - 1.5 million $km^2$, however these changes are not
827   statistically significant. These results are comparable with the results from the CMIP6 models
828   (Davy and Outten, 2020). In the 2030-2050 March mean the sea-ice extent is projected to be

829   925 000 km$^2$ lower in the Eclipse ensemble (statistically significant), while the CMIP6
830   ensemble projects a decrease of 991 000 km$^2$ (not statistically significant) A much larger
831   decrease is projected for the 2030-2050 September mean, being 2.6 million km$^2$ and 2.3
832   million km$^2$ in Eclipse and CMIP6 ensembles, respectively. As seen in Figure 12, the Eclipse
833   ensemble predicts an up to 90% lower September sea-ice fraction in a band marking the
834   maximum retreat of the sea ice line at the end of the summer, while the changes simulated by
835   the CMIP6 ensemble are not statistically significant on 95% level (therefore not shown in
836   Figure 11), which can be attributed to the single ensemble member per scenario in the CMIP6
837   ensemble, as well as the not significant changes in the near-surface temperatures (not shown).
838   In March (Figure S3), the Eclipse ensemble simulated a decrease in maximum sea-ice extent
839   at the end of winter over the northern Pacific, while the CMIP6 ensemble did not show any
840   statistically significant changes in sea-ice. In addition, the Eclipse ensemble shows a decrease
841   over the north Atlantic close to Greenland. All simulations show a similar and statistically
842   significant decrease in annual mean sea-ice extent (Figure S4 over the central Arctic, with the
843   CMIP6 ensemble showing also some increase in the sea-ice extent over the Canadian Arctic,
844   that is largest in SSP3-7.0.

845

846   The retreat in sea-ice extent also led to an increase of oceanic emissions of DMS and sea-salt
847   (Figure S5); however, the increases are not significant on a 95% significance level. The
848   simulated increase, in particular for the DMS emissions, is slightly larger in the Eclipse
849   ensemble compared to the CMIP6 ensemble, due to a larger decrease of sea-ice extent in the
850   Eclipse ensemble. Also note that GISS-E2.1 is using prescribed and fixed maps of DMS
851   concentration in the ocean. When ocean locations that are year-round under sea-ice at present
852   get exposed, the DMS that would exist in that sea water is not included in the simulations,
853   likely underestimating the increased flux of DMS into the atmosphere as the sea ice retreats.

854

855   4. Summary and Conclusions

856

857   The GISS-E2.1 earth system model has been used to simulate the recent past (1990-2014)
858   and future (2015-2050) aerosol burdens and their climate impacts over the Arctic. An
859   ensemble of seventeen simulations has been conducted, using historical and future
860   anthropogenic emissions and projections from CMIP6 and ECLIPSE V6b, the latter
861   supporting the ongoing Arctic Monitoring and Assessment Programme.

862

863   The evaluation of the recent past simulations shows underestimates of Arctic surface aerosol
864   levels by up to 50%, with the smallest biases calculated for the simulations where winds are
865   nudged, and sea-surface temperature and sea-ice are prescribed (AMIP-type: atmosphere-
866   only). An exception is $SO_4^{2-}$, where the nudged Eclipse AMIP simulation had the highest
867   bias, due to the high cloud bias that leads to more in-cloud sulfate production from $SO_2$. The
868   model skill analyses indicate slightly better performance of the CMIP6 version of the GISS-
869   E2.1 model in simulating both the aerosol levels and climate parameters compared to the
870   Eclipse version. In addition, the underestimations in summer time cloud fraction suggests
871   missing sources of aerosols, in particular the local marine sources. GISS-E2.1 does not
872   include marine VOC emissions except for DMS, which are suggested to be important for the

summer time cloud properties over the Arctic (Ornella et al., 2011; Karl et al., 2013; Schmale et al., 2021). Results also suggest that the underestimation of both absorbing and scattering aerosol levels can partly cancel out their impacts on $RF_{ARI}$ and near-surface temperatures as the temperatures are very well reproduced by the model.

From 2015 onwards, all simulations, except for the worst case CMIP6 scenario SSP3-7.0, show a statistically significant decrease in the Arctic BC, OA and $SO_4^{2-}$ burdens, with the CMIP6 ensemble simulating larger aerosol burdens Eclipse, while the Eclipse ensemble shows larger reductions (10-60%) in Arctic aerosol burdens compared to the reduction simulated by the CMIP6 ensemble (10-45%). The largest burden reductions are calculated by the highly ambitious emission reductions in the two ensembles; i.e. the Eclipse MFR (25-60%) and the CMIP6 SSP1-2.6 (25-45%).

The present-day (1990-2010 mean) CMIP6 and Eclipse simulations calculated an aerosol radiative forcing due to aerosol-radiation interactions ($RF_{ARI}$ ) of -0.32 to -0.35 W m$^{-2}$. For the same period, the atmosphere only (AMIP) Eclipse simulations calculated a much larger negative $RF_{ARI}$ of -0.47 W m$^{-2}$. This smaller $RF_{ARI}$ by the coupled simulations is mainly due to larger BC burdens in the coupled simulations, leading to more positive forcing, which is amplified by the larger albedo effect due to larger sea-ice extent simulated in the coupled simulations. In the 2030-2050 period, the Eclipse ensemble simulated a $RF_{ARI}$ -0.39±0.01 W m$^{-2}$, of which -0.24±0.01 W m$^{-2}$ are attributed to the anthropogenic aerosols (BC, OA, $SO_4^{2-}$ and $NO_3^-$). For the same period, the worst case CMIP6 scenario (SSP3-7.0) simulated a similar $RF_{ARI}$ (-0.35 W m$^{-2}$) compared to the 1990-2010 mean , while large emission reductions led to a more negative $RF_{ARI}$ (-0.40 W m$^{-2}$), mainly due to decrease in the positive forcing of the BC aerosols. Overall, the Eclipse ensemble simulated slightly larger changes in the $RF_{ARI}$ over the 2015-2050 period, relative to the 1990-2010 mean, compared to the CMIP6 ensemble, which can be attributed to the larger reductions in burdens in the Eclipse ensemble. The differences between the two ensembles are further attributed to differences in the BC and $SO_4^{2-}$ forcings. The results suggest that the different anthropogenic emission projections lead to only small differences in how the $RF_{ARI}$ will evolve in the future over the Arctic.

The future scenarios with the largest aerosol reductions, i.e. MFR in the Eclipse and SSP1-2.6 in the CMIP6 ensemble projects a largest warming and sea-ice retreat. The Eclipse ensemble shows a slightly larger warming of 2030-2050 mean surface air temperatures compared to the 1990-2010 mean warming (2.1 to 2.5 °C) compared to that from the CMIP6 ensemble (1.9 °C to 2-2 °C). Larger warming in the Eclipse ensemble also resulted in a slightly larger reduction in sea-ice extent (-1.5 to -1.7 million km$^{-2}$ in CLE and MFR, respectively) in 2030-2050 mean compared to the reduction in the CMIP6 scenario (-1.3 to -1.6 million km$^{-2}$ in SSP1.2-6 and SSP3-7.0, respectively). However, the changes simulated by the two ensembles are within one standard deviation of each other.

The overall results showed that the aerosol burdens will substantially decrease in the short- to mid-term future, implying improvements in impacts on human health and ecosystems.

However, the impacts of aerosols on the radiative forcing can be amplified by the sea-ice extent. Results also show that even the scenarios with largest emission reductions, i.e. Eclipse MFR and CMIP6 SSP1-2.6, lead to similar impact on the future Arctic surface air temperatures and sea-ice loss compared to scenarios with very little mitigation such as the CMIP6 SSP3-7.0, exacerbating the dominant role played by well-mixed greenhouse gases and underlining the importance of continued greenhouse gas reductions.

*Author contributions.* UI coordinated the study, conducted the model simulations, as well as model evaluation and analyses of the simulations, and wrote the manuscript. KT and GF supported the model simulations and processing of the Eclipse V6b emissions for the GISS-E2.1 model. JPF contributed to the plotting of the spatial distributions by further developing the autoimage R package (French, 2017). RM prepared and provided the AOD measurements, as well as the surface air temperature, sea surface temperature and sea-ice data. MAT prepared the cloud observation data. CHW prepared the Arctic surface aerosol measurement data. KvS coordinated the experimental setup for the Eclipse simulations in the framework of the ongoing AMAP assessment. ZG prepared and provided the Eclipse V6b anthropogenic emissions. HS and DCT prepared the Villum Research Station aerosol data. JB and PL contributed to analyses of aerosols and climate parameters, respectively, and manuscript writing. All authors contributed to the analyses and interpretation of the results, as well as contributing to the writing of the manuscript.

*Competing Interests.* The authors declare that they have no conflict of interest.

*Special issue statement.* This article is part of the special issue "Arctic climate, air quality, and health impacts from short-lived climate forcers (SLCFs): contributions from the AMAP Expert Group".

*Acknowledgements.* This paper was developed as part of the Arctic Monitoring Assessment Programme (AMAP), AMAP 2021Assessment: Arctic climate, air quality, and health impacts from short-lived climate forcers (SLCFs). HadISST data were obtained from https://www.metoffice.gov.uk/hadobs/hadisst/ and are © British Crown Copyright, Met Office, provided under a Non-Commercial Government Licence http://www.nationalarchives.gov.uk/doc/non-commercial-government-licence/version/2/. UDel_AirT_Precip data provided by the NOAA/OAR/ESRL PSL, Boulder, Colorado, USA, from their Web site at https://psl.noaa.gov/. Alert sulfate data are from Sangeeta and EC & OA data from Lin Huang, respectively, as part of Canadian Aerosol Baseline Measurement (CABM) program at ECCC and would like to thank operators & technicians for collection of filters, calibration and analysis and Canadian Forces Services Alert for the operation of the military base. These datasets are also available on Global Atmospheric Watch program, World Data Center for aerosols, EBAS database (http://ebas.nilu.no/default.aspx).Aside from Alert, Canada's surface air quality data are from the National Atmospheric Pollutant Surveillance network (NAPS: https://open.canada.ca/data/en/dataset/1b36a356-defd-4813-acea-47bc3abd859b).

Fairbanks aerosol measurements are from William Simpson and KC Nattinger. Aside from Fairbanks, Alaskan measurements are from the IMPROVE network. IMPROVE is a collaborative association of state, tribal, and federal agencies, and international partners. The US Environmental Protection Agency is the primary funding source, with contracting and research support from the National Park Service. The Air Quality Group at the University of California, Davis is the central analytical laboratory, with ion analysis provided by Research Triangle Institute, and carbon analysis provided by Desert Research Institute. European measurements are from the EMEP network, and obtained from the EBAS database (http://ebas.nilu.no). Other European data include the Gruvebadet measurements, for which we acknowledge Mauro Mazzola (mauro.mazzola@cnr.it), Stefania Gilardoni (stefania.gilardoni@cnr.it), and Angelo Lupi (angelo.lupi@cnr.it) from the Institute of Polar Sciences fo Gruvabadet eBC measurements; and Rita Traversi (rita.traversi@unifi.it), Mirko Severi (mirko.severi@unifi.it), and  Silvia Becagli (silvia.becagli@unifi.it) from University of Florence http://www.isac.cnr.it/~radiclim/CCTower/ ?Data:Aerosol; the Zeppelin datasets, for which we acknowledge Vito Vitale and Angelo Lupi (also available on http://ebas.nilu.no); and the Villum Station datasets (www.villumresearchstation.dk) from Henrik Skov (hsk@envs.au.dk; also available in http://ebas.nilo.no). The AERONET AOD measurements were obtained from NASA's Goddard Space Flight Center (https://aeronet.gsfc.nasa.gov/new_web/index.html). The authors acknowledge Dr. L. Sogacheva and AEROSAT team for satellite based merged AOD data.

*Financial support.* This research has been supported by the Aarhus University Interdisciplinary Centre for Climate Change (iClimate) OH fund (no. 2020-0162731), the FREYA project, funded by the Nordic Council of Ministers (grant agreement no. MST-227-00036 and MFVM-2019-13476), and the EVAM-SLCF funded by the Danish Environmental Agency (grant agreement no. MST-112-00298). KT and GF thank the NASA Modeling, Analysis and Prediction program (MAP) for support. ZK was financially supported by the EU-funded Action on Black Carbon in the Arctic (EUA-BCA) under the EU Partnership Instrument. JPF was partially supported by NSF award 1915277.

**References**

Abbatt, J. P. D., Leaitch, W. R., Aliabadi, A. A., Bertram, A. K., Blanchet, J.-P., Boivin-Rioux, A., Bozem, H., Burkart, J., Chang, R. Y. W., Charette, J., Chaubey, J. P., Christensen, R. J., Cirisan, A., Collins, D. B., Croft, B., Dionne, J., Evans, G. J., Fletcher, C. G., Galí, M., Ghahremaninezhad, R., Girard, E., Gong, W., Gosselin, M., Gourdal, M., Hanna, S. J., Hayashida, H., Herber, A. B., Hesaraki, S., Hoor, P., Huang, L., Hussherr, R., Irish, V. E., Keita, S. A., Kodros, J. K., Köllner, F., Kolonjari, F., Kunkel, D., Ladino, L. A., Law, K., Levasseur, M., Libois, Q., Liggio, J., Lizotte, M., Macdonald, K. M., Mahmood, R., Martin, R. V., Mason, R. H., Miller, L. A., Moravek, A., Mortenson, E., Mungall, E. L., Murphy, J. G., Namazi, M., Norman, A.-L., O'Neill, N. T., Pierce, J. R., Russell, L. M., Schneider, J., Schulz, H., Sharma, S., Si, M., Staebler, R. M., Steiner, N. S., Thomas, J. L., von Salzen, K.,

1001 Wentzell, J. J. B., Willis, M. D., Wentworth, G. R., Xu, J.-W., and Yakobi-Hancock, J. D.:
1002 Overview paper: New insights into aerosol and climate in the Arctic, Atmos. Chem. Phys.,
1003 19, 2527–2560, https://doi.org/10.5194/acp-19-2527-2019, 2019.

1004 AMAP 2021 Assessment: Arctic climate, air quality, and health impacts from short-lived
1005 climate forcers (SLCFs).

1006 AMAP, 2015. AMAP Assessment 2015: Black carbon and ozone as Arctic climate forcers.
1007 Arctic Monitoring and Assessment Programme (AMAP), Oslo, Norway. vii + 116 pp.

1008 Amann, M., Bertok, I., Borken-Kleefeld, J., Cofala, J., Heyes, C., Höglund-Isaksson, L.,
1009 Klimont, Z., Nguyen, B., Posch, M., Rafaj, P., Sandler, R., Schöpp, W., Wagner, F.,
1010 Winiwarter, W.: Cost-effective control of air quality and greenhouse gases in Europe:
1011 Modeling and policy applications. Environmental Modelling & Software, 26, (12), 1489-
1012 1501, 2011.

1013 Ångström, A.: On the Atmospheric Transmission of Sun Radiation and on Dust in the Air.
1014 Geografiska Annaler, 11, 156-166. doi:10.2307/519399, 1929.

1015 Bauer, S. E., Tsigaridis, K., Faluvegi, G.,Kelley, M., Lo, K. K., & Miller, R. L.,et al.:
1016 Historical (1850–2014) aerosol evolution and role on climate forcing using the GISS
1017 ModelE2.1contribution to CMIP6. Journal ofAdvances in Modeling Earth Systems,12,
1018 e2019MS001978, https://doi.org/10.1029/2019MS001978, 2020.

1019 Bauer, S.E., and Koch, D.: Impact of heterogeneous sulfate formation at mineral dust
1020 surfaces on aerosol loads and radiative forcing in the Goddard Institute for Space Studies
1021 general circulation model. J. Geophys. Res., 110, D17202, doi:10.1029/2005JD005870, 2005.

1022 Bond, T.C., Doherty, S.J., Fahey, D.W., Forster, P.M. , Berntsen, T., De Angelo, B.J.,
1023 Flanner, M.G., Ghan, S., Karcher, B., Koch, D., Kinne, S., Kondo, Y., Quiinn, P.K., Sarofim,
1024 M.C., Schultz, M.G., Schulz, M., Venkataraman, C., Zhang, H., Zhang, S., Bellouin, N.,
1025 Guttikunda, S.K., Hopke, P.K., Jacobson, M.Z., Kaiser, J.W., Klimont, Z., Lohmann, U.,
1026 Schwarz, J.P., Shindell, D., Storelvmo, T., Warren, S.G., Zender, C.S.: Bounding the role of
1027 black carbon in the climate system: a scientific assessment, J. Geophys. Res. Atmos., 118
1028 (11), 5380-5552, 10.1002/jgrd.50171, 2013.

1029 Bond, T. C., D. G. Streets, K. F. Yarber, S. M. Nelson, J. H. Woo, and Z. Klimont: A
1030 technology-based global inventory of black and organic carbon emissions from combustion,
1031 J. Geophys. Res., 109, D14203, doi:10.1029/2003JD003697, 2014.

1032 Boy, M., Thomson, E. S., Acosta Navarro, J.-C., Arnalds, O., Batchvarova, E., Bäck, J.,
1033 Berninger, F., Bilde, M., Brasseur, Z., Dagsson-Waldhauserova, P., Castarède, D., Dalirian,
1034 M., de Leeuw, G., Dragosics, M., Duplissy, E.-M., Duplissy, J., Ekman, A. M. L., Fang, K.,
1035 Gallet, J.-C., Glasius, M., Gryning, S.-E., Grythe, H., Hansson, H.-C., Hansson, M., Isaksson,
1036 E., Iversen, T., Jonsdottir, I., Kasurinen, V., Kirkevåg, A., Korhola, A., Krejci, R.,
1037 Kristjansson, J. E., Lappalainen, H. K., Lauri, A., Leppäranta, M., Lihavainen, H.,
1038 Makkonen, R., Massling, A., Meinander, O., Nilsson, E. D., Olafsson, H., Pettersson, J. B.
1039 C., Prisle, N. L., Riipinen, I., Roldin, P., Ruppel, M., Salter, M., Sand, M., Seland, Ø., Seppä,
1040 H., Skov, H., Soares, J., Stohl, A., Ström, J., Svensson, J., Swietlicki, E., Tabakova, K.,

1041 Thorsteinsson, T., Virkkula, A., Weyhenmeyer, G. A., Wu, Y., Zieger, P., and Kulmala, M.:
1042 Interactions between the atmosphere, cryosphere, and ecosystems at northern high latitudes,
1043 Atmos. Chem. Phys., 19, 2015–2061, https://doi.org/10.5194/acp-19-2015-2019, 2019.

1044 Breider, T. J., Mickley, L. J., Jacob, D. J., Ge, C., Wang, J., Payer Sulprizio, M., Croft, B.,
1045 Ridley, D. A., McConnell, J. R., Sharma, S., Husain, L., Dutkiewicz, V. A., Eleftheriadis, K.,
1046 Skov, H. and Hopke, P. K.: Multidecadal trends in aerosol radiative forcing over the Arctic:
1047 Contribution of changes in anthropogenic aerosol to Arctic warming since 1980, J. Geophys.
1048 Res. Atmos., 122(6), 3573–3594, doi:10.1002/2016JD025321, 2017.

1049 Burnett, R., Chena, H., Szyszkowicza, M., Fann, N., Hubbell, B., Pope III, C. A., Apte, J. S.,
1050 Brauer, M., Cohen, A., Weichenthal, S., Coggins, J., Di Q., Brunekreef B., Frostad, J.,  Lim,
1051 S. S., Kan, H., Walker, K. D., Thurston, G. D., Hayes, R. B.,  Lim, C. C., Turner, M. C.,
1052 Jerrett, M., Krewski, D., Gapstur, S. M., Diver, W. R., Ostro, B., Goldberg, D., Crouse,  D.
1053 L., Martin, R. V., Peters, P., Pinault, L., Tjepkema, M., van Donkelaar, M., Villeneuve,  P. J.,
1054 Miller, A. B., Yin, P., Zhou, M., Wang, L.,  Janssen, N. A. H., Marra, M., Atkinson, R. W.,
1055 Tsang, H., Thach, T. Q., Cannon, J. B., Allen, R. T.,  Hart, J. E., Laden, F., Cesaroni, G.,
1056 Forastiere, F., Weinmayr, G., Jaensch, A., Nagel, G., Concin, H. and Spadar, J. V., Global
1057 estimates of mortality associated with long term exposure to outdoor fine particulate matter.
1058 Proceedings of the National Academy of Sciences, 38 (115), pp. 9592–9597. doi:
1059 10.1073/pnas.1803222115. 2018.

1060 Clarke, A.D., and Noone, K.J.: Soot in the Arctic snowpack: A cause for perturbations in
1061 radiative transfer, Atmos. Environ., 19, 2045– 2053, 1985.

1062 Collins, W. J., Lamarque, J.-F., Schulz, M., Boucher, O., Eyring, V., Hegglin, M. I.,
1063 Maycock, A., Myhre, G., Prather, M., Shindell, D., and Smith, S. J.: AerChemMIP:
1064 quantifying the effects of chemistry and aerosols in CMIP6, Geosci. Model Dev., 10, 585–
1065 607, https://doi.org/10.5194/gmd-10-585-2017, 2017.

1066 Davy, R., and Outten, S.: The Arctic Surface Climate in CMIP6: Status and Developments
1067 since CMIP5, *J. Climate*, 33 (18), 8047–8068, https://doi.org/10.1175/JCLI-D-19-0990.1,
1068 2020.

1069 Dumont, M., Brun, E., Picard, G. et al.: Contribution of light-absorbing impurities in snow to
1070 Greenland's darkening since 2009. Nature Geosci 7, 509–512,
1071 https://doi.org/10.1038/ngeo2180, 2014.

1072 Eck, T.F., B.N.Holben, J.S.Reid, O.Dubovik, A.Smirnov, N.T.O'Neill, I.Slutsker, and
1073 S.Kinne: Wavelength dependence of the optical depth of biomass burning, urban and desert
1074 dust aerosols, J. Geophys. Res., 104, 31 333-31 350, 1999.

1075 Eckhardt, S., Quennehen, B., Olivié, D. J. L., Berntsen, T. K., Cherian, R., Christensen, J. H.,
1076 Collins, W., Crepinsek, S., Daskalakis, N., Flanner, M., Herber, A., Heyes, C., Hodnebrog,
1077 Ø., Huang, L., Kanakidou, M., Klimont, Z., Langner, J., Law, K. S., Lund, M. T., Mahmood,
1078 R., Massling, A., Myriokefalitakis, S., Nielsen, I. E., Nøjgaard, J. K., Quaas, J., Quinn, P. K.,
1079 Raut, J.-C., Rumbold, S. T., Schulz, M., Sharma, S., Skeie, R. B., Skov, H., Uttal, T., von
1080 Salzen, K., and Stohl, A.: Current model capabilities for simulating black carbon and sulfate
1081 concentrations in the Arctic atmosphere: a multi-model evaluation using a comprehensive

measurement data set, Atmos. Chem. Phys., 15, 9413–9433, https://doi.org/10.5194/acp-15-9413-2015, 2015.

Eyring, V., Bony, S., Meehl, G. A., Senior, C. A., Stevens, B., Stouffer, R. J., and Taylor, K. E.: Overview of the Coupled Model Intercomparison Project Phase 6 (CMIP6) experimental design and organization, Geosci. Model Dev., 9, 1937–1958, https://doi.org/10.5194/gmd-9-1937-2016, 2016.

Feng, L., Smith, S. J., Braun, C., Crippa, M., Gidden, M. J., Hoesly, R., Klimont, Z., van Marle, M., van den Berg, M., and van der Werf, G. R.: The generation of gridded emissions data for CMIP6, Geosci. Model Dev., 13, 461–482, https://doi.org/10.5194/gmd-13-461-2020, 2020.

Flanner, M.G., Zender, C.S., Randerson, J.T., and Rasch, P.J.: Present-day climate forcing and response from blackcarbon in snow, J. Geophys. Res., 112, D11202, doi:10.1029/2006JD008003, 2007.

French, J.P.: autoimage: Multiple Heat Maps for Projected Coordinates, The R Journal, 9 (1), 284-297, 2017.

Gagné, M.-È., Gillett, N.P., and Fyfe, J. C.: Impact of aerosolemission controls on futureArctic sea ice cover, Geo-phys. Res. Lett., 42, 8481–8488,doi:10.1002/2015GL065504, 2015.

Gery, M., Whitten, G.Z., Killus, J.P., and Dodge, M.C.: A photochemical kinetics mechanism for urban and regional scale computer modelling, J.Geophys.Res., 94, 18925-18956, 1989.

Gidden, M. J., Riahi, K., Smith, S. J., Fujimori, S., Luderer, G., Kriegler, E., van Vuuren, D. P., van den Berg, M., Feng, L., Klein, D., Calvin, K., Doelman, J. C., Frank, S., Fricko, O., Harmsen, M., Hasegawa, T., Havlik, P., Hilaire, J., Hoesly, R., Horing, J., Popp, A., Stehfest, E., and Takahashi, K.: Global emissions pathways under different socioeconomic scenarios for use in CMIP6: a dataset of harmonized emissions trajectories through the end of the century, Geosci. Model Dev., 12, 1443–1475, https://doi.org/10.5194/gmd-12-1443-2019, 2019.

Gidden, M. J., Fujimori, S., van den Berg, M., Klein, D., Smith, S. J., van Vuuren, D. P., and Riahi, K.: A methodology and implementation of automated emissions harmonization for use in Integrated Assessment Models, Environ. Modell. Softw., 105, 187–200, 2018.

Graversen R, Langen P.L.: On the Role of the Atmospheric Energy Transport in 2xCO2-Induced Polar Amplification in CESM1. Journal of Climate, 32(13), 3941-3956, 2019.

Gryspeerdt, E., Goren, T., Sourdeval, O., Quaas, J., Mülmenstädt, J., Dipu, S., Unglaub, C., Gettelman, A., and Christensen, M.: Constraining the aerosol influence on cloud liquid water path, Atmos. Chem. Phys., 19, 5331–5347, https://doi.org/10.5194/acp-19-5331-2019, 2019.

Hansen, J., M. Sato, R. Ruedy, L. Nazarenko, A. Lacis, G.A. Schmidt, G. Russell, I. Aleinov, M. Bauer, S. Bauer, N. Bell, B. Cairns, V. Canuto, M. Chandler, Y. Cheng, A. Del Genio, G. Faluvegi, E. Fleming, A. Friend, T. Hall, C. Jackman, M. Kelley, N.Y. Kiang, D. Koch, J. Lean, J. Lerner, K. Lo, S. Menon, R.L. Miller, P. Minnis, T. Novakov, V. Oinas, J.P.

Perlwitz, J. Perlwitz, D. Rind, A. Romanou, D. Shindell, P. Stone, S. Sun, N. Tausnev, D. Thresher, B. Wielicki, T. Wong, M. Yao, and S. Zhang: Efficacy of climate forcings. J. Geophys. Res., 110, D18104, doi:10.1029/2005JD005776, 2005.

Hoesly, R. M., Smith, S. J., Feng, L., Klimont, Z., Janssens-Maenhout, G., Pitkanen, T., Seibert, J. J., Vu, L., Andres, R. J., Bolt, R. M., Bond, T. C., Dawidowski, L., Kholod, N., Kurokawa, J.-I., Li, M., Liu, L., Lu, Z., Moura, M. C. P., O'Rourke, P. R., and Zhang, Q.: Historical (1750–2014) anthropogenic emissions of reactive gases and aerosols from the Community Emissions Data System (CEDS), Geosci. Model Dev., 11, 369–408, https://doi.org/10.5194/gmd-11-369-2018, 2018.

Holben B.N., T.F.Eck, I.Slutsker, D.Tanre, J.P.Buis, A.Setzer, E.Vermote, J.A.Reagan, Y.Kaufman, T.Nakajima, F.Lavenu, I.Jankowiak, and A.Smirnov: AERONET - A federated instrument network and data archive for aerosol characterization, Rem. Sens. Environ., 66, 1-16, 1998.

Höglund-Isaksson, L., Gómez-Sanabria, A., Klimont, Z., Rafaj, P., Schöpp, W.: Technical potentials and costs for reducing global anthropogenic methane emissions in the 2050 timeframe –results from the GAINS model. Environmental Research Communications, 2 (2), 2020.

International Energy Agency (IEA): World Energy Outlook 2018, 661 pp., ISBN 978-92-64-30677-6, 2018.

IPCC, 2014: Climate Change 2014: Synthesis Report. Contribution of Working Groups I, II and III to the Fifth Assessment Report of the Intergovernmental Panel on Climate Change [Core Writing Team, R.K. Pachauri and L.A. Meyer (eds.)]. IPCC, Geneva, Switzerland, 151 pp.

IPCC, 2013: Climate Change 2013: The Physical Science Basis. Contribution of Working Group I to the Fifth Assessment Report of the Intergovernmental Panel on Climate Change [Stocker, T.F., D. Qin, G.-K. Plattner, M. Tignor, S.K. Allen, J. Boschung, A. Nauels, Y. Xia, V. Bex and P.M. Midgley (eds.)]. Cambridge University Press, Cambridge, United Kingdom and New York, NY, USA, 1535 pp.

Jacobson, M. Z.: Strong radiative heating due to the mixing state of black carbon in the atmospheric aerosols, Nature, 409, 695–698, 2001.

Karl, M., Leck, C., Coz, E., Heintzenberg, J. Marine nanogels as a source of atmospheric nanoparticles in the high Arctic, Geophysical Research Letters, 40, 14, 3738-3743, doi.org/10.1002/grl.50661, 2013.

Karlsson, K.-G., Devasthale, A: Inter-Comparison and Evaluation of the Four Longest Satellite-Derived Cloud Climate Data Records: CLARA-A2, ESA Cloud CCI V3, ISCCP-HGM, and PATMOS-x. Remote Sens. 2018, 10, 1567.

Karlsson, K.-G., Anttila, K., Trentmann, J., Stengel, M., Fokke Meirink, J., Devasthale, A., Hanschmann, T., Kothe, S., Jääskeläinen, E., Sedlar, J., Benas, N., van Zadelhoff, G.-J., Schlundt, C., Stein, D., Finkensieper, S., Håkansson, N., and Hollmann, R.: CLARA-A2: the second edition of the CM SAF cloud and radiation data record from 34 years of global

AVHRR data, Atmos. Chem. Phys., 17, 5809–5828, https://doi.org/10.5194/acp-17-5809-2017, 2017.

Karlsson, Karl-Göran; Anttila, Kati; Trentmann, Jörg; Stengel, Martin; Meirink, Jan Fokke; Devasthale, Abhay; Hanschmann, Timo; Kothe, Steffen; Jääskeläinen, Emmihenna; Sedlar, Joseph; Benas, Nikos; van Zadelhoff, Gerd-Jan; Schlundt, Cornelia; Stein, Diana; Finkensieper, Stephan; Håkansson, Nina; Hollmann, Rainer; Fuchs, Petra; Werscheck, Martin (2017): CLARA-A2: CM SAF cLoud, Albedo and surface RAdiation dataset from AVHRR data - Edition 2, Satellite Application Facility on Climate Monitoring, https://doi.org/10.5676/EUM_SAF_CM/CLARA_AVHRR/V002 (last access: October 26th 2020).

Kay, J., and L'Ecuyer, T.: Observational constraints on Arctic Ocean clouds and radiative fluxes during the early 21st century. Journal of Geophysical Research: Atmospheres. 118. 10.1002/jgrd.50489, 2013.

Keil, P., Mauritsen, T., Jungclaus, J. *et al.* Multiple drivers of the North Atlantic warming hole. *Nat. Clim. Chang.* 10, 667–671, https://doi.org/10.1038/s41558-020-0819-8, 2020.

Kelley, M., Schmidt, G. A., Nazarenko, L. S., Bauer, S. E., Ruedy, R., Russell, G. L., et al.: GISS-E2.1: Configurations and climatology. Journal of Advances in Modeling Earth Systems, 12, e2019MS002025. https://doi.org/10.1029/2019MS002025, 2020.

Klimont, Heyes, Rafaj, Schoepp, Purohit, Cofala, Hoglund-Isaksson, Wagner,...et al. Global scenarios of anthropogenic emissions of air pollutants: ECLIPSE (in preparation for GMD)

Klimont, Z., Kupiainen, K., Heyes, C., Purohit, P., Cofala, J., Rafaj, P., Borken-Kleefeld, J., and Schöpp, W.: Global anthropogenic emissions of particulate matter including black carbon, Atmos. Chem. Phys., 17, 8681–8723, https://doi.org/10.5194/acp-17-8681-2017, 2017.

Lamarque, J.-F., Bond, T. C., Eyring, V., Granier, C., Heil, A., Klimont, Z., Lee, D., Liousse, C., Mieville, A., Owen, B., Schultz, M. G., Shindell, D., Smith, S. J., Stehfest, E., Van Aardenne, J., Cooper, O. R., Kainuma, M., Mahowald, N., McConnell, J. R., Naik, V., Riahi, K., and van Vuuren, D. P.: Historical (1850–2000) gridded anthropogenic and biomass burning emissions of reactive gases and aerosols: methodology and application, Atmos. Chem. Phys., 10, 7017–7039, https://doi.org/10.5194/acp-10-7017-2010, 2010.

Law, K. S., Stohl, A., Quinn, P. K., Brock, C. A., Burkhart, J. F., Paris, J., Ancellet, G., Singh, H. B., Roiger, A., Schlager, H., Dibb, J., Jacob, D. J., Arnold, S. R., Pelon, J., and Thomas, J. L. Arctic Air Pollution: New Insights from POLARCAT-IPY, Bulletin of the American Meteorological Society, 95(12), 1873-1895, 2014.

Lelieveld, J., Klingmüller, K., Pozzer, A., Pöschl, U., Fnais, M., Daiber, A., Münzel, T. Cardiovascular disease burden from ambient air pollution in Europe reassessed using novel hazard ratio functions. European Heart Journal 40, 1590-1596. https://doi.org/10.1093/eurheartj/ehz135, 2019.

1199  Lenssen, N. J. L., Schmidt, G. A., Hansen, J. E., Menne, M. J., Persin, A., Ruedy, R. and
1200  Zyss, D.: Improvements in the GISTEMP Uncertainty Model. Journal of Geophysical
1201  Research: Atmospheres 124: 6307-6326 10.1029/2018jd029522, 2019.

1202  Lewinschal, A., Ekman, A. M. L., Hansson, H. C., Sand, M., Berntsen, T. K., & Langner, J.
1203  (2019). Local and remote temperature response of regional SO2 emissions. Atmospheric
1204  Chemistry and Physics, 19, 2385– 2403. https://doi.org/10.5194/acp-19-2385-2019

1205  Lund, M. T., Myhre, G., Haslerud, A. S., Skeie, R. B., Griesfeller, J., Platt, S. M., Kumar, R.,
1206  Myhre, C. L., and Schulz, M.: Concentrations and radiative forcing of anthropogenic aerosols
1207  from 1750 to 2014 simulated with the Oslo CTM3 and CEDS emission inventory, Geosci.
1208  Model Dev., 11, 4909–4931, https://doi.org/10.5194/gmd-11-4909-2018, 2018.

1209  Lund, M. T., Berntsen, T. K., and Samset, B. H.: Sensitivity of black carbon concentrations
1210  and climate impact to aging and scavenging in OsloCTM2-M7, Atmos. Chem. Phys., 17,
1211  6003–6022, https://doi.org/10.5194/acp-17-6003-2017, 2017.

1212  Mahmood, R., von Salzen, K., Norman, A.-L., Galí, M., and Levasseur, M.: Sensitivity of
1213  Arctic sulfate aerosol and clouds to changes in future surface seawater dimethylsulfide
1214  concentrations, Atmos. Chem. Phys., 19, 6419–6435, https://doi.org/10.5194/acp-19-6419-
1215  2019, 2019.

1216  Markowicz, K.M.,Lisok, J., Xian, P.: Simulation of long-term direct aerosol radiative forcing
1217  over the arctic within the framework of the iAREA project. Atmospheric Environment, 244,
1218  117882, 2021.

1219  Menary, M.B., Wood, R.A.: An anatomy of the projected North Atlantic warming hole in
1220  CMIP5 models. *Clim Dyn* 50, 3063–3080, https://doi.org/10.1007/s00382-017-3793-8, 2018.

1221  Menon, S., and Rotstayn, L.: The radiative influence of aerosol effects on liquid-phase
1222  cumulus and stratus clouds based on sensitivity studies with two climate models, Clim. Dyn.,
1223  27, 345– 356, 2006.

1224  Miller, R.L., G.A. Schmidt, L. Nazarenko, S.E. Bauer, M. Kelley, R. Ruedy, G.L. Russell, A.
1225  Ackerman, I. Aleinov, M. Bauer, R. Bleck, V. Canuto, G. Cesana, Y. Cheng, T.L. Clune, B.
1226  Cook, C.A. Cruz, A.D. Del Genio, G.S. Elsaesser, G. Faluvegi, N.Y. Kiang, D. Kim, A.A.
1227  Lacis, A. Leboissetier, A.N. LeGrande, K.K. Lo, J. Marshall, E.E. Matthews, S. McDermid,
1228  K. Mezuman, L.T. Murray, V. Oinas, C. Orbe, C. Pérez García-Pando, J.P. Perlwitz, M.J.
1229  Puma, D. Rind, A. Romanou, D.T. Shindell, S. Sun, N. Tausnev, K. Tsigaridis, G. Tselioudis,
1230  E. Weng, J. Wu, and M.-S. Yao: CMIP6 historical simulations (1850-2014) with GISS-E2.1.
1231  J. Adv. Model. Earth Syst., in press, doi:10.1029/2019MS002034, 2020.

1232  Miller, R.L., G.A. Schmidt, and D.T. Shindell: Forced annular variations in the 20th century
1233  Intergovernmental Panel on Climate Change Fourth Assessment Report models. J. Geophys.
1234  Res., 111, D18101, doi:10.1029/2005JD006323, 2006.

1235  Myhre, G., D. Shindell, F.-M. Bréon, W. Collins, J. Fuglestvedt, J. Huang, D. Koch, J.-F.
1236  Lamarque, D. Lee, B. Mendoza, T. Nakajima, A. Robock, G. Stephens, T. Takemura, and H.
1237  Zhang: Anthropogenic and natural radiative forcing. In Climate Change 2013: The Physical
1238  Science Basis. Contribution of Working Group I to the Fifth Assessment Report of the

1239 Intergovernmental Panel on Climate Change. T.F. Stocker, D. Qin, G.-K. Plattner, M. Tignor,
1240 S.K. Allen, J. Doschung, A. Nauels, Y. Xia, V. Bex, and P.M. Midgley, Eds. Cambridge
1241 University Press, pp. 659-740, doi:10.1017/CBO9781107415324.018, 2013.

1242 Orellana, M.V., Matrai, P,A., Leck, C., Rauschenberg, C.D., Lee, A.M., and Coz, E., Marine
1243 microgels as a source of cloud condensation nuclei in the high Arctic, Proceedings of the
1244 National Academy of Sciences, 108 (33) 13612-13617,
1245 https://doi.org/10.1073/pnas.1102457108, 2011.

1246 Platnick, S., S. A. Ackerman, M. D. King, K. Meyer, W. P. Menzel, R. E. Holz, B. A. Baum,
1247 and P. Yang: MODIS atmosphere L2 cloud product (06_L2), NASA MODIS Adaptive
1248 Processing System, Goddard Space Flight Center, 2015.

1249 Quinn, P.K., Shaw, G., Andrews, E., Dutton, E.G., Ruoho-Airola, T., Gong, S.L. Arctic haze:
1250 current trends and knowledge gaps, Tellus B: Chemical and Physical Meteorology, 59:1, 99-
1251 114, DOI: 10.1111/j.1600-0889.2006.00236.x, 2007.

1252 Rao, S., Klimont, Z., Smith, S.J., Van Dingenen, R., Dentener, F., Bouwman, L., Riahia, K.,
1253 Amann, M., Bodirsky, B.L., van Vuuren, D.P., Reis, L.A., Calvin, K., Drouet, L., Fricko, O.,
1254 Fujimori, S., Gernaat, D., Havlik, P., Harmsen, M., Hasegawa, T., Heyes, C., Hilaire, J.,
1255 Luderer, G., Masui, T., Stehfest, E., Strefler, J., van der Slui, S., Tavonil, M.: Future air
1256 pollution in the Shared Socio-economic Pathways. Global Environmental Change, 42, 346-
1257 358, 2017.

1258 Rayner, N. A., D. E. Parker, E. B. Horton, C. K. Folland, L. V. Alexander, D. P. Rowell, E.
1259 C. Kent, and A. Kaplan, Global analyses of sea surface temperature, sea ice, and night marine
1260 air temperature since the late nineteenth century, J. Geophys. Res.,108(D14), 4407,
1261 doi:10.1029/2002JD002670, 2003.

1262 Ren, L., Yang, Y., Wang, H., Zhang, R., Wang, P., and Liao, H.: Source attribution of Arctic
1263 black carbon and sulfate aerosols and associated Arctic surface warming during 1980–2018,
1264 Atmos. Chem. Phys., 20, 9067–9085, https://doi.org/10.5194/acp-20-9067-2020, 2020.

1265 Reynolds, R.W., Rayner, N.A., Smith, T.M., Stokes, D.C., and Wang, W. An improved in
1266 situ and satellite SST analysis for climate. J. Climate, 15, 1609-1625, 2002.

1267 Riahi, K.,van Vuuren, D.P., Kriegler, E., Edmonds, J., O'Neil, B.C., Fujimori, S., Bauer, N.,
1268 Calvin, K., Dellink, R., Fricko, O., Lutz, W., Popp, A., Cuaresma, C.J., KC, S., Leimbach,
1269 M., Jiang, L., Kram, T., Rao, S., Emmerling, J., Ebi, K., Hasegawa, T., Havlik, P.,
1270 Humpenöder, F., Da Silva, L.A:, Smith, S., Stehfest[E,,] Bosetti, V., Eom, J., Gernaat, D.,
1271 Masui, T., Rogelj, J., Strefler, J., Drouet, L., Krey, V., Luderer, G., Harmsen, M., Takahashi,
1272 K., Baumstark, L., Doelman, J.C., Kainuma, M., Klimont, Z., Marangoni, G., Lotze-Campen,
1273 H., Obersteiner, M., Tabeau, A., Tavoni, M.: The Shared Socioeconomic Pathways and their
1274 energy, land use, and greenhouse gas emissions implications: An overview. Global
1275 Environmental Change, 42, 153-168, 2017.

1276 Samset, B. H., Sand, M., Smith, C. J., Bauer, S. E., Forster, P. M., Fuglestvedt, J. S., Osprey,
1277 S., & Schleussner, C.-F.: Climate impacts from a removal of anthropogenic aerosol
1278 emissions. Geophysical Research Letters, 45. https://doi.org/10.1002/2017GL076079, 2018.

Sand, M., T. K. Berntsen, K. von Salzen, M. G. Flanner, J. Langner, and D. G. Victor: Response of arctic temperature to changes in emissions of short-lived climate forcers, Nat. Clim. Change, 6, 286–289, doi:10.1038/nclimate2880, 2015.

Sayer, A. M., Hsu, N. C., Lee, J., Kim, W. V., Dubovik, O., Dutcher, S. T. et al.: Validation of SOAR VIIRS over-water aerosol retrievals and context within the global satellite aerosol data record. Journal of Geophysical Research: Atmospheres, 123, 13,496–13,526, https://doi.org/10.1029/2018JD029465, 2018.

Sayer, A. M. and Knobelspiesse, K. D.: How should we aggregate data? Methods accounting for the numerical distributions, with an assessment of aerosol optical depth, Atmos. Chem. Phys., 19, 15023–15048, https://doi.org/10.5194/acp-19-15023-2019, 2019.

Schacht, J., Heinold, B., Quaas, J., Backman, J., Cherian, R., Ehrlich, A., Herber, A., Huang, W. T. K., Kondo, Y., Massling, A., Sinha, P. R., Weinzierl, B., Zanatta, M., and Tegen, I.: The importance of the representation of air pollution emissions for the modeled distribution and radiative effects of black carbon in the Arctic, Atmos. Chem. Phys., 19, 11159–11183, https://doi.org/10.5194/acp-19-11159-2019, 2019.

Schmale, J., Zieger, P., Ekman, A.M.L. Aerosols in current and future Arctic climate. Nature Climate Change, 11, 95–105, https://doi.org/10.1038/s41558-020-00969-5, 2021.

Schutgens, N. A. J.: Site representativity of AERONET and GAW remotely sensed aerosol optical thickness and absorbing aerosol optical thickness observations, Atmos. Chem. Phys., 20, 7473–7488, https://doi.org/10.5194/acp-20-7473-2020, 2020a.

Schutgens, N., Sayer, A. M., Heckel, A., Hsu, C., Jethva, H., de Leeuw, G., Leonard, P. J. T., Levy, R. C., Lipponen, A., Lyapustin, A., North, P., Popp, T., Poulson, C., Sawyer, V., Sogacheva, L., Thomas, G., Torres, O., Wang, Y., Kinne, S., Schulz, M., and Stier, P.: An AeroCom/AeroSat study: Intercomparison of Satellite AOD Datasets for Aerosol Model Evaluation, Atmos. Chem. Phys. Discuss., https://doi.org/10.5194/acp-2019-1193, in review, 2020b.

Semmler, T., Pithan, F., Jung, T.: Quantifying two-way influences between the Arctic and mid-latitudes through regionally increased CO2 concentrations in coupled climate simulations, *Climate Dynamics*, 54, 3307–3321, 2020.

Serreze, M.C., Francis, J.A. The Arctic Amplification Debate. Climatic Change 76, 241–264, https://doi.org/10.1007/s10584-005-9017-y, 2006.

Shindell, D. T., Lamarque, J.-F., Schulz, M., Flanner, M., Jiao, C., Chin, M., Young, P. J., Lee, Y. H., Rotstayn, L., Mahowald, N., Milly, G., Faluvegi, G., Balkanski, Y., Collins, W. J., Conley, A. J., Dalsoren, S., Easter, R., Ghan, S., Horowitz, L., Liu, X., Myhre, G., Nagashima, T., Naik, V., Rumbold, S. T., Skeie, R., Sudo, K., Szopa, S., Takemura, T., Voulgarakis, A., Yoon, J.-H., and Lo, F.: Radiative forcing in the ACCMIP historical and future climate simulations, Atmos. Chem. Phys., 13, 2939–2974, https://doi.org/10.5194/acp-13-2939-2013, 2013.

Shindell, D., J.C.I. Kuylenstierna, E. Vignati, R. van Dingenen, M. Amann, Z. Klimont, S.C. Anenberg, N. Muller, G. Janssens-Maenhout, F. Raes, J. Schwartz, G. Faluvegi, L. Pozzoli,

K. Kupiainen, L. Höglund-Isaksson, L. Emberson, D. Streets, V. Ramanathan, K. Hicks, N.T.K. Oanh, G. Milly, M. Williams, V. Demkine, and D. Fowler, Simultaneously mitigating near-term climate change and improving human health and food security. Science, 335, 183-189, doi:10.1126/science.1210026, 2012.

Shindell, D., and G. Faluvegi,: Climate response to regional radiative forcing during the twentieth century. Nature Geosci., 2, 294-300, doi:10.1038/ngeo473, 2009.

Shindell, D.: Local and remote contributions to Arctic warming, Geophysical Research Letters – Climate, 34, L14704, https://doi.org/10.1029/2007GL030221, 2007.

Sogacheva, L., Popp, T., Sayer, A. M., Dubovik, O., Garay, M. J., Heckel, A., Hsu, N. C., Jethva, H., Kahn, R. A., Kolmonen, P., Kosmale, M., de Leeuw, G., Levy, R. C., Litvinov, P., Lyapustin, A., North, P., Torres, O., and Arola, A.: Merging regional and global aerosol optical depth records from major available satellite products, Atmos. Chem. Phys., 20, 2031–2056, https://doi.org/10.5194/acp-20-2031-2020, 2020.

Skeie, R. B., Berntsen, T., Myhre, G., Pedersen, C. A., Ström, J., Gerland, S., and Ogren, J. A.: Black carbon in the atmosphere and snow, from pre-industrial times until present, Atmos. Chem. Phys., 11, 6809–6836, https://doi.org/10.5194/acp-11-6809-2011, 2011.

Stephens, G. L., and Coauthors,: THE CLOUDSAT MISSION AND THE A-TRAIN: A New Dimension of Space-Based Observations of Clouds and Precipitation. Bull. Amer. Meteor. Soc., 83, 1771–1790, https://doi.org/10.1175/BAMS-83-12-1771, 2002.

Stjern, C. W., Samset, B. H., Myhre, G.,Forster, P. M., Hodnebrog, Ø. Andrews,T., Boucher, O., Faluvegi, G., Iversen, T., Kasoar, M., Kharin, V., Kirkevåg, A., Lamarque, J.-F., Olivie, D., Richardson, T, Shawki, D., Shindell, D., Smith, C.J., Takemura, T., Voulgarakis, A. Rapid adjustments cause weak surface temperature response to increased black carbon concentrations. Journal of Geophysical Research: Atmospheres, 122,11,462–11,481. https://doi.org/10.1002/2017JD02732, 2017.

Stohl, A., Aamaas, B., Amann, M., Baker, L. H., Bellouin, N., Berntsen, T. K., Boucher, O., Cherian, R., Collins, W., Daskalakis, N., Dusinska, M., Eckhardt, S., Fuglestvedt, J. S., Harju, M., Heyes, C., Hodnebrog, Ø., Hao, J., Im, U., Kanakidou, M., Klimont, Z., Kupiainen, K., Law, K. S., Lund, M. T., Maas, R., MacIntosh, C. R., Myhre, G., Myriokefalitakis, S., Olivié, D., Quaas, J., Quennehen, B., Raut, J.-C., Rumbold, S. T., Samset, B. H., Schulz, M., Seland, Ø., Shine, K. P., Skeie, R. B., Wang, S., Yttri, K. E., and Zhu, T.: Evaluating the climate and air quality impacts of short-lived pollutants, Atmos. Chem. Phys., 15, 10529–10566, https://doi.org/10.5194/acp-15-10529-2015, 2015.

Stohl, A. Characteristics of atmospheric transport into the Arctic troposphere, J. Geophys. Res., 111, D11306, doi:10.1029/2005JD006888, 2006.

Stuecker, M.F., Bitz, C.M., Armour, K.C., Proistosescu, C., Kang, S.M., Xie, S.-P., Kim, D., McGregor, S., Zhang, W., Zhao, S., Cai, W., Dong, Y., Jin, F.-F.: Polar amplification dominated by local forcing and feedbacks, *Nature Climate Change*, 8, 1076–1081, 2018.

Takemura, T., Suzuki, K. Weak global warming mitigation by reducing black carbon emissions. Scientific Reports, 9, 4419 (2019). https://doi.org/10.1038/s41598-019-41181-6

1359 Thomas, M. A., Devasthale, A., Tjernström, M., and Ekman, A. M. L. The relation between
1360 aerosol vertical distribution and temperature inversions in the Arctic in winter and spring.
1361 Geophysical Research Letters, 46, 2836– 2845. https://doi.org/10.1029/2018GL081624,
1362 2019.

1363 Thomas, J.L., et al.: Fostering multidisciplinary research on interactions between chemistry,
1364 biology, and physics within the coupled cryosphere-atmosphere system. Elem Sci Anth, 7:
1365 58. DOI: https://doi.org/10.1525/elementa.396, 2019.

1366 Tsigaridis, K., and M. Kanakidou,: Secondary organic aerosol importance in the future
1367 atmosphere. Atmos. Environ., 41, 4682-4692, doi:10.1016/j.atmosenv.2007.03.045, 2007.

1368 Turnock, S. T., Allen, R. J., Andrews, M., Bauer, S. E., Deushi, M., Emmons, L., Good, P.,
1369 Horowitz, L., John, J. G., Michou, M., Nabat, P., Naik, V., Neubauer, D., O'Connor, F. M.,
1370 Olivié, D., Oshima, N., Schulz, M., Sellar, A., Shim, S., Takemura, T., Tilmes, S., Tsigaridis,
1371 K., Wu, T., and Zhang, J.: Historical and future changes in air pollutants from CMIP6
1372 models, Atmos. Chem. Phys., 20, 14547–14579, https://doi.org/10.5194/acp-20-14547-2020,
1373 2020.

1374 van Marle, M. J. E., Kloster, S., Magi, B. I., Marlon, J. R., Daniau, A.-L., Field, R. D.,
1375 Arneth, A., Forrest, M., Hantson, S., Kehrwald, N. M., Knorr, W., Lasslop, G., Li, F.,
1376 Mangeon, S., Yue, C., Kaiser, J. W., and van der Werf, G. R.: Historic global biomass
1377 burning emissions for CMIP6 (BB4CMIP) based on merging satellite observations with
1378 proxies and fire models (1750–2015), Geosci. Model Dev., 10, 3329–3357,
1379 https://doi.org/10.5194/gmd-10-3329-2017, 2017.

1380 Wei, J., Peng, Y., Mahmood, R., Sun, L., and Guo, J.: Intercomparison in spatial distributions
1381 and temporal trends derived from multi-source satellite aerosol products, Atmos. Chem.
1382 Phys., 19, 7183–7207, https://doi.org/10.5194/acp-19-7183-2019, 2019.

1383 Westervelt, D. M., Horowitz, L. W., Naik, V., Golaz, J.-C., & Mauzerall, D. L.: Radiative
1384 forcing and climate response to projected 21st century aerosol decreases. Atmospheric
1385 Chemistry and Physics, 15, 12,681– 12,703. https://doi.org/10.5194/acp-15-12681-2015,
1386 2015.

1387 Willis, M. D., Leaitch, W. R., &Abbatt, J. P.: Processescontrolling the composition
1388 andabundance of Arctic aerosol.Reviews of Geophysics, 56, 621–671.
1389 https://doi.org/10.1029/2018RG000602, 2018.

1390 Willmott, C. J. and K. Matsuura,: Terrestrial Air Temperature and Precipitation: Monthly and
1391 Annual Time Series (1950 - 1999), 2001.
1392 (http://climate.geog.udel.edu/~climate/html_pages/README.ghcn_ts2.html, (last access:
1393 October 26th)

**Tables**

Table 1. GISS-E2.1 simulations carried out in the Eclipse and CMIP6 ensembles.

| Simulations | Description | No. Ensemble | Period |
|---|---|---|---|
| NINT_Cpl | No tracers- Coupled | 1 | 1850-2014 |
| Eclipse_AMIP | AMIP OMA | 1 | 1995-2014 |
| Eclipse_AMIP_NCEP | AMIP OMA – winds nudged to NCEP | 1 | 1995-2014 |
| Eclipse_CplHist | OMA – Coupled | 3 | 1990-2014 |
| Eclipse_Cpl_CLE | OMA – Coupled | 3 | 2015-2050 |
| Eclipse_Cpl_MFR | OMA – Coupled | 3 | 2020-2050 |
| CMIP6_Cpl_Hist | OMA – Coupled | 1 | 1850-2014 |
| CMIP6_Cpl_SSP1-2.6 | OMA – Coupled | 1 | 2015-2050 |
| CMIP6_Cpl_SSP2-4.5 | OMA – Coupled | 1 | 2015-2050 |
| CMIP6_Cpl_SSP3-7.0 | OMA – Coupled | 1 | 2015-2050 |
| CMIP6_Cpl_SSP3-7.0-lowNTCF | OMA – Coupled | 1 | 2015-2050 |

Table 2. Annual mean normalized mean bias (*NMB:%*) and correlation coefficients (*r*) for the recent past simulations in the GISS-E2.1 model ensemble during 1995-2014 for BC, OA, $SO_4^{2-}$ and 2008/2009-2014 for AOD550 from AERONET and satellites.

| | BC | | OA | | $SO_4^{2-}$ | | AOD_aero | | AOD_sat | |
|---|---|---|---|---|---|---|---|---|---|---|
| Model | *NMB* | *r* | *NMB* | *r* | *NMB* | *r* | *NMB* | *r* | *NMB* | *r* |
| AMAP_OnlyAtm. | -67.32 | 0.27 | -35.46 | 0.54 | -49.83 | 0.65 | -33.28 | -0.07 | -0.48 | 0.00 |
| AMAP_OnlyAtm_NCEP | -57.00 | 0.26 | -7.80 | 0.56 | -52.70 | 0.74 | -41.99 | 0.02 | -0.55 | 0.13 |
| AMAP_CplHist (x3) | -64.11 | 0.42 | -19.07 | 0.58 | -49.39 | 0.71 | -43.28 | 0.04 | -0.56 | 0.07 |
| CMIP6_Cpl_Hist | -49.90 | 0.26 | 13.14 | 0.69 | -39.81 | 0.70 | -39.86 | 0.05 | -0.53 | 0.11 |

Table 3a. Annual normalized mean biases (*NMB*: %) and correlation coefficients (*r*) for the recent past simulations in the GISS-E2.1 model ensemble in 1995-2014 for surface air temperature ($T_{surf}$) and sea surface temperature (SST) in units of °C, and precipitation (Precip), and sea-ice fraction (Sea-ice).

| | $T_{surf}$ | | Precip | | SST | | Sea-ice | |
|---|---|---|---|---|---|---|---|---|
| Model | *NMB* | *r* | *NMB* | *r* | *NMB* | *r* | *NMB* | *r* |
| NINT | -0.08 | 1.00 | -52.68 | 0.88 | -88.87 | 0.99 | 12.14 | 1.00 |
| AMAP_OnlyAtm. | -19.73 | 1.00 | -50.33 | 0.89 | -68.00 | 0.99 | -2.56 | 1.00 |
| AMAP_OnlyAtm_NCEP | -14.74 | 1.00 | -53.19 | 0.90 | -68.00 | 0.99 | -2.56 | 1.00 |
| AMAP_CplHistx3 | -3.35 | 1.00 | -53.06 | 0.86 | -87.51 | 0.99 | 11.35 | 1.00 |
| CMIP6_Cpl_Hist | -1.22 | 1.00 | -53.96 | 0.85 | -88.53 | 0.98 | 12.56 | 0.99 |

Table 3b. Annual mean normalized mean biases (*NMB*: %) and correlation coefficients (*r*) for the recent past simulations in the GISS-E2.1 model ensemble in 1995-2014 for total cloud fraction (Cld Frac), liquid water path (LWP), and ice water path (IWP) in units of %.

| | Cld Frac | | LWP | | IWP | |
|---|---|---|---|---|---|---|
| Model | *NMB* | *r* | *NMB* | *r* | *NMB* | *r* |
| NINT | 20.95 | -0.67 | 70.55 | -0.89 | -56.06 | 0.53 |
| AMAP_OnlyAtm. | 23.78 | -0.81 | 57.52 | -0.96 | -58.53 | -0.18 |
| AMAP_OnlyAtm_NCEP | 24.83 | -0.79 | 14.19 | -0.91 | -70.32 | -0.64 |
| AMAP_CplHistx3 | 21.64 | -0.65 | 70.99 | -0.91 | -55.74 | 0.48 |
| CMIP6_Cpl_Hist | 21.49 | -0.65 | 69.18 | -0.91 | -56.28 | 0.40 |

Table 4. Trends in Arctic BC, OA and $SO_4^{2-}$ burdens in the near-past (1990-2014) and future (2030-2050) as calculated by the GISS-E2.1. The bold numbers indicate the trends that are statistically significant on a 95% significance level.

| | BC | | OA | | $SO_4^{2-}$ | |
|---|---|---|---|---|---|---|
| | 1990-2014 | 2015-2050 | 1990-2014 | 2015-2050 | 1990-2014 | 2015-2050 |
| Eclipse_AMIP | **-0.026** | | 0.030 | | **-0.886** | |
| Eclipse_AMIP_NCEP | **-0.021** | | 0.112 | | **-0.939** | |
| Eclipse_CplHist_3xEns | **-0.026** | | -0.006 | | **-1.332** | |
| Eclipse_CplCLE_3xEns | | **-0.024** | | **-0.201** | | **-0.143** |
| Eclipse_CplMFR_3xEns | | **-0.043** | | **-0.367** | | **-0.146** |
| CEDS_Cpl_Hist | 0.007 | | 0.121 | | **-1.093** | |
| CEDS_Cpl_SSP126 | | **-0.068** | | **-0.715** | | **-0.935** |
| CEDS_Cpl_SSP245 | | **-0.047** | | **-0.384** | | **-0.465** |
| CEDS_Cpl_SSP370 | | **-0.004** | | **-0.062** | | **0.027** |
| CEDS_Cpl_SSP370-lowNTCF | | **-0.051** | | **-0.642** | | **-0.567** |

Table 5. Arctic BC, OA and $SO_4^{2-}$ burdens in 1990-2010 and 2030-2050 periods as calculated by the GISS-E2.1.

| | BC | | OA | | $SO_4^{2-}$ | |
|---|---|---|---|---|---|---|
| | 1990-2010 | 2030-2050 | 1990-2010 | 2030-2050 | 1990-2010 | 2030-2050 |
| Eclipse_AMIP | 3.52 | | 50.70 | | 95.10 | |
| Eclipse_AMIP_NCEP | 3.49 | | 57.31 | | 93.93 | |
| Eclipse_CplHist_3xEns | 3.75 | | 55.55 | | 93.59 | |
| Eclipse_CplCLE_3xEns | | 2.58 | | 48.95 | | 63.52 |
| Eclipse_CplMFR_3xEns | | 1.44 | | 40.39 | | 53.35 |
| CEDS_Cpl_Hist | 3.64 | | 67.48 | | 99.11 | |
| CEDS_Cpl_SSP126 | | 2.05 | | 50.41 | | 53.99 |
| CEDS_Cpl_SSP245 | | 2.65 | | 59.43 | | 69.71 |
| CEDS_Cpl_SSP370 | | 4.08 | | 68.81 | | 83.26 |
| CEDS_Cpl_SSP370-lowNTCF | | 2.94 | | 56.05 | | 69.72 |

Table 6a. RF$_{ARI}$ for BC, OA, SO$_4^{2-}$ and NO$_3^-$ aerosols in 1990-2010 and 2030-2050 periods as calculated by the GISS-E2.1.

| | BC | | OA | | SO$_4^{2-}$ | | NO$_3^-$ | |
| --- | --- | --- | --- | --- | --- | --- | --- | --- |
| | 1990-2010 | 2030-2050 | 1990-2010 | 2030-2050 | 1990-2010 | 2030-2050 | 1990-2010 | 2030-2050 |
| NINT_Cpl | 0.20 | | -0.05 | | -0.33 | | -0.01 | |
| Eclipse_AMIP | 0.20 | | -0.06 | | -0.39 | | -0.02 | |
| Eclipse_AMIP_NCEP | 0.19 | | -0.08 | | -0.39 | | -0.04 | |
| Eclipse_CplHist_3xEns | 0.23 | | -0.05 | | -0.38 | | -0.03 | |
| Eclipse_CplCLE_3xEns | | 0.17 | | -0.07 | | -0.27 | | -0.07 |
| Eclipse_CplMFR_3xEns | | 0.09 | | -0.07 | | -0.22 | | -0.04 |
| CEDS_Cpl_Hist | 0.23 | | -0.06 | | -0.40 | | -0.04 | |
| CEDS_Cpl_SSP126 | | 0.13 | | -0.07 | | -0.22 | | -0.10 |
| CEDS_Cpl_SSP245 | | 0.19 | | -0.08 | | -0.29 | | -0.09 |
| CEDS_Cpl_SSP370 | | 0.28 | | -0.09 | | -0.34 | | -0.06 |
| CEDS_Cpl_SSP370-lowNTCF | | 0.20 | | -0.07 | | -0.28 | | -0.09 |

Table 6b. RF$_{ARI}$ for total and anthropogenic aerosols in 1990-2010 and 2030-2050 periods as calculated by the GISS-E2.1.

| | Aerosols Total | | Anthropogenic Aerosols | |
| --- | --- | --- | --- | --- |
| | 1990-2010 | 2030-2050 | 1990-2010 | 2030-2050 |
| NINT_Cpl | -0.35 | | -0.19 | |
| Eclipse_AMIP | -0.46 | | -0.27 | |
| Eclipse_AMIP_NCEP | -0.47 | | -0.32 | |
| Eclipse_CplHist_3xEns | -0.32 | | -0.22 | |
| Eclipse_CplCLE_3xEns | | -0.39 | | -0.24 |
| Eclipse_CplMFR_3xEns | | -0.39 | | -0.23 |
| CEDS_Cpl_Hist | -0.35 | | -0.26 | |
| CEDS_Cpl_SSP126 | | -0.40 | | -0.26 |
| CEDS_Cpl_SSP245 | | -0.41 | | -0.27 |
| CEDS_Cpl_SSP370 | | -0.35 | | -0.21 |
| CEDS_Cpl_SSP370-lowNTCF | | -0.38 | | -0.24 |

Table 7. Trends in near surface temperature ($T_{surf}$) and annual mean sea-ice extent in 1990-2010 and 2030-2050 periods as calculated by the GISS-E2.1. The bold numbers indicate the changes in 2030-2050 mean compared to the 1990-2010 mean that are statistically significant on a 95% significance level.

| | $T_{surf}$ (°C decade$^{-1}$) | | Sea-ice ($10^3$ km$^2$) | |
|---|---|---|---|---|
| | 1990-2010 | 2030-2050 | 1990-2010 | 2030-2050 |
| Observed | **0.19** | | **-28.36** | |
| NINT_Cpl | **0.88** | | **-60.10** | |
| Eclipse_AMIP | **0.52** | | **-28.65** | |
| Eclipse_AMIP_NCEP | **0.62** | | **-29.47** | |
| Eclipse_CplHist_3xEns | **0.52** | | **-37.89** | |
| Eclipse_CplCLE_3xEns | | **0.45** | | **-37.212** |
| Eclipse_CplMFR_3xEns | | **0.55** | | **-41.33** |
| CEDS_Cpl_Hist | **0.10** | | **-69.79** | |
| CEDS_Cpl_SSP126 | | **0.31** | | **-23.21** |
| CEDS_Cpl_SSP245 | | **0.38** | | **-24.28** |
| CEDS_Cpl_SSP370 | | **0.50** | | **-39.18** |
| CEDS_Cpl_SSP370-lowNTCF | | **0.31** | | **-21.89** |

Table 8. Near surface temperature ($T_{surf}$) and September-mean sea-ice extent in1990-2010 and 2030-2050 periods as calculated by the GISS-E2.1. The bold numbers indicate the changes in 2030-2050 mean compared to the 1990-2010 mean that are statistically significant on a 95% significance level.

| | $T_{surf}$ (°C) | | September Sea-ice ($10^3$ km$^2$) | |
|---|---|---|---|---|
| | 1990-2010 | 2030-2050 | 1990-2010 | 2030-2050 |
| NINT_Cpl | -8.39 | | | |
| Eclipse_AMIP | -6.54 | | | |
| Eclipse_AMIP_NCEP | -7.10 | | | |
| Eclipse_CplHist_3xEns | -8.13 | | 1.56 | |
| Eclipse_CplCLE_3xEns | | **-6.06** | | **1.32** |
| Eclipse_CplMFR_3xEns | | **-5.79** | | **1.31** |
| CEDS_Cpl_Hist | -8.52 | | 1.60 | |
| CEDS_Cpl_SSP126 | | **-6.64** | | 1.44 |
| CEDS_Cpl_SSP245 | | **-6.37** | | 1.37 |
| CEDS_Cpl_SSP370 | | **-6.33** | | 1.37 |
| CEDS_Cpl_SSP370-lowNTCF | | **-6.56** | | 1.38 |

**Figures**
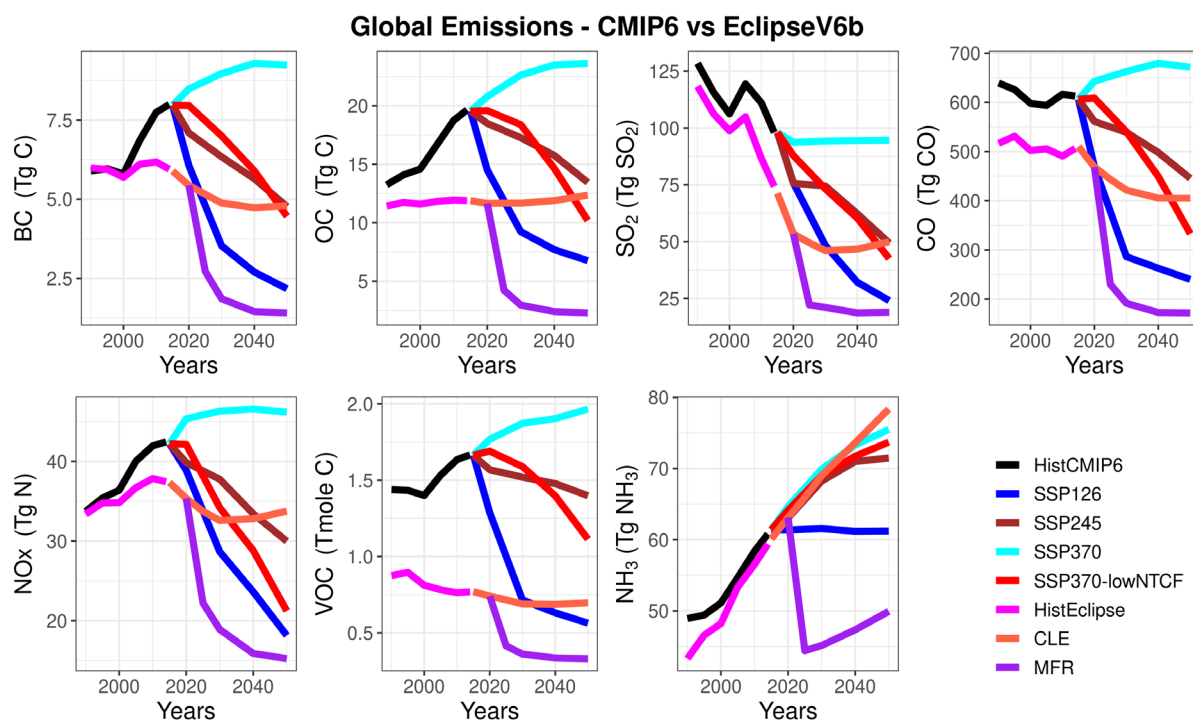
Figure 1. Global recent past and future CMIP6 and Eclipse V6b anthropogenic emissions for different pollutants and scenarios.
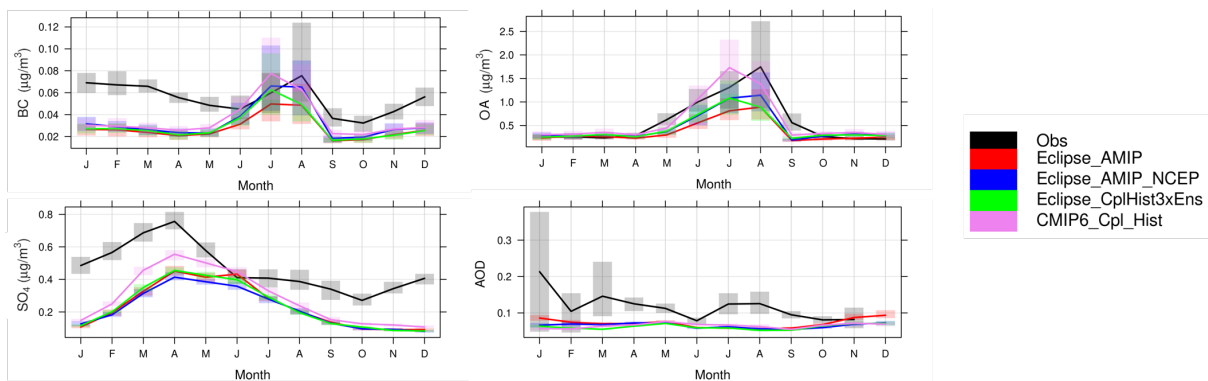
Figure 2. Observed and simulated Arctic climatological (1995-2014) monthly BC, OA, $SO_4^{2-}$, and AERONET AOD at 550nm (2008/09-14), along with the interannual variation shown in bars. The data presents monthly accumulated timeseries for all stations that are merged together.
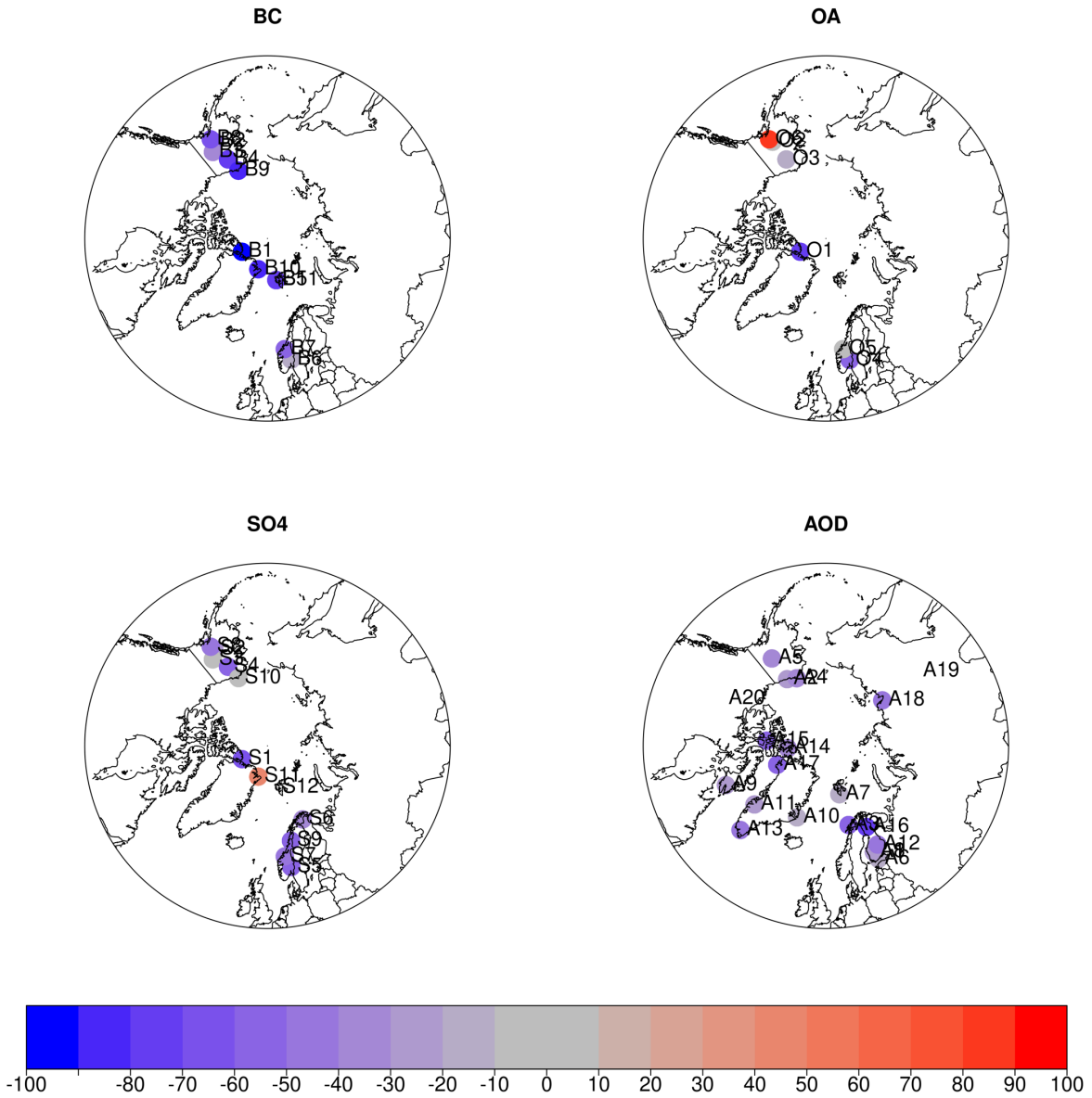
Figure 3. Spatial distribution of normalized mean bias (*NMB*, in %) for climatological mean (1995-2014) BC, OA, $SO_4^{2-}$ and AOD at monitoring stations, calculated as the mean of all recent past simulations.
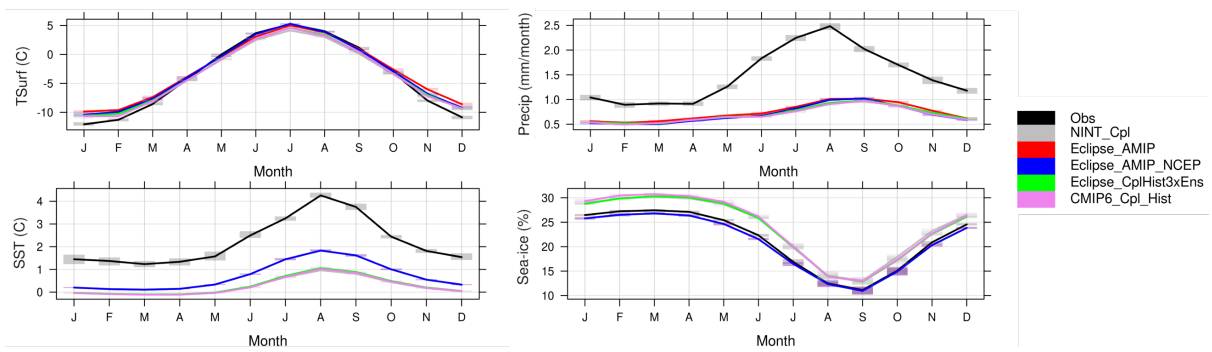
Figure 4. Observed and simulated Arctic climatological (1995-2014) surface air temperature, precipitation, sea surface temperature, and sea-ice, along with the interannual variation shown in bars. Obs denote UDel dataset for surface air temperature and precipitation, and HADISST for sea surface temperature and sea-ice extent. Note that the two AMIP runs (blue and red lines) for the SST and sea-ice are on top of each other as they use that data to run, as input.
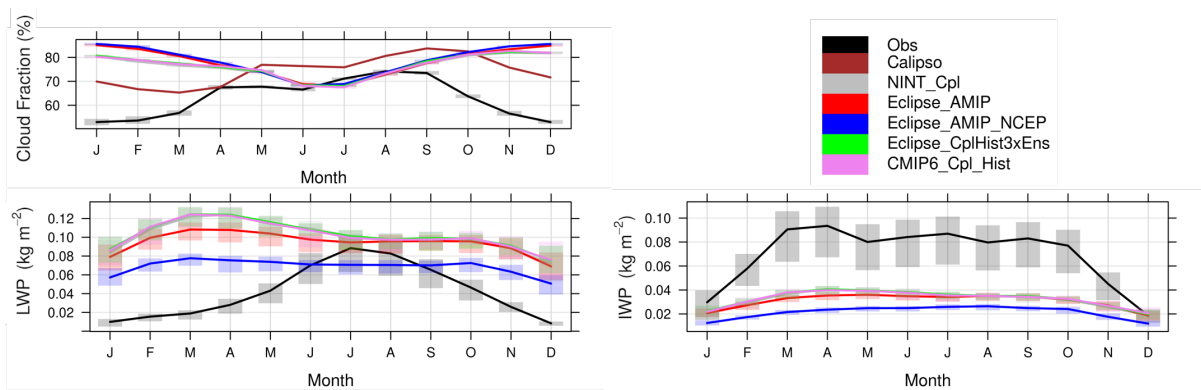
Figure 5. Observed and simulated Arctic climatological total cloud fraction (1995-2014 mean), liquid water path (2007-2014 mean), and ice water path (2007-2014 mean) , along with the interannual variation shown in bars. Obs denote Clara-A2 for the cloud fractions and CloudSat for the LWP and IWP.
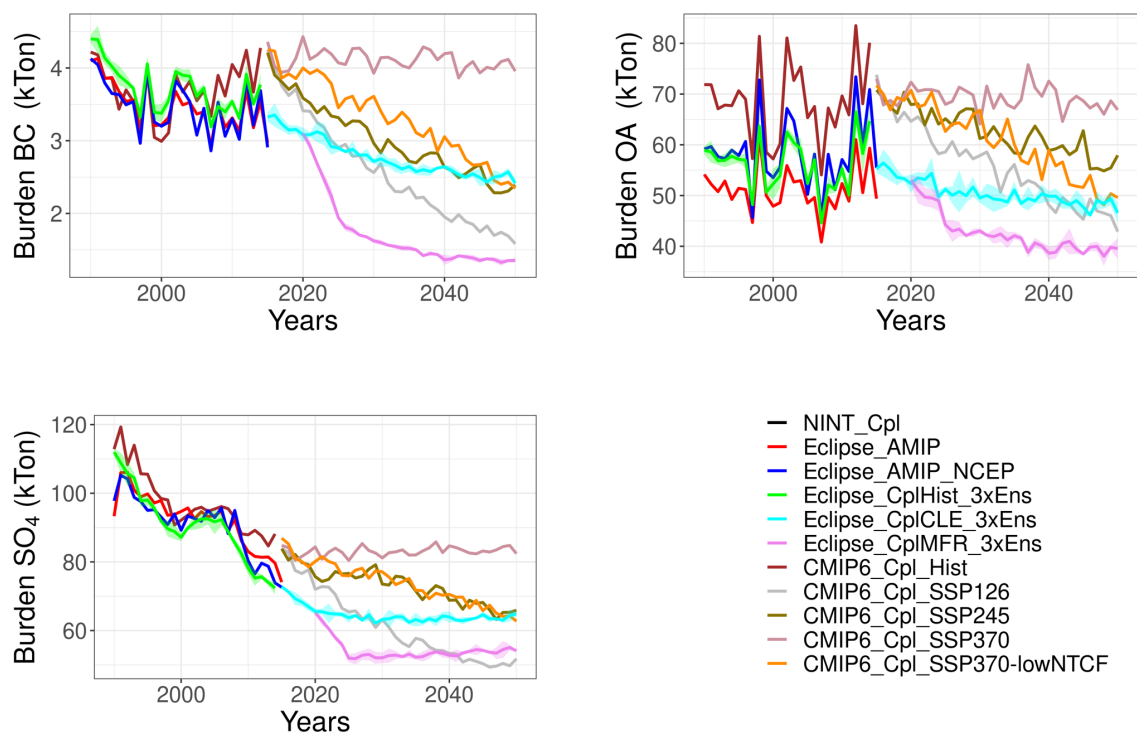
Figure 6. Arctic BC, OA and SO$_4^{2-}$ burdens in 1990-2050 as calculated by the GISS-E2.1 ensemble.
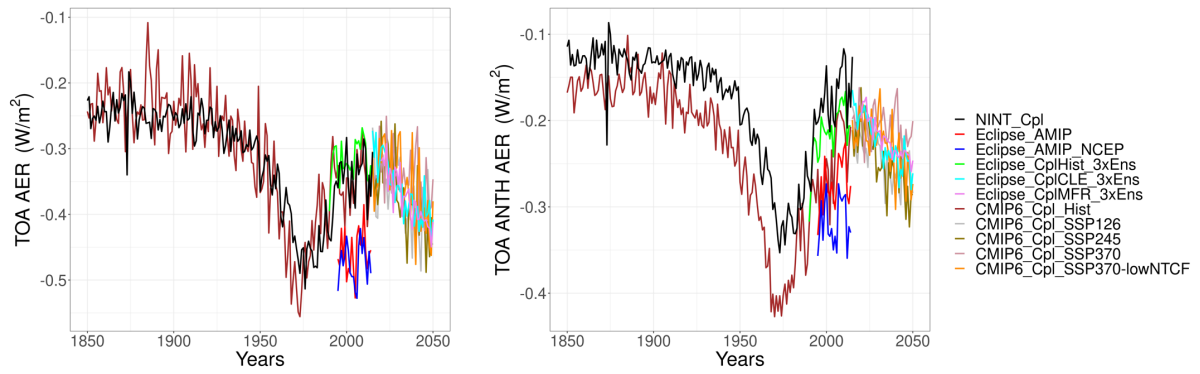
Figure 7. Arctic RF$_{ARI}$ from anthropogenic and natural aerosols (BC+OA+SO$_4^{2-}$+NO$_3^-$ +Dust+SSA), and only anthropogenic aerosols (BC+OA+SO$_4^{2-}$+NO$_3^-$) in 1850-2050 as calculated by the full GISS-E2.1 ensemble.
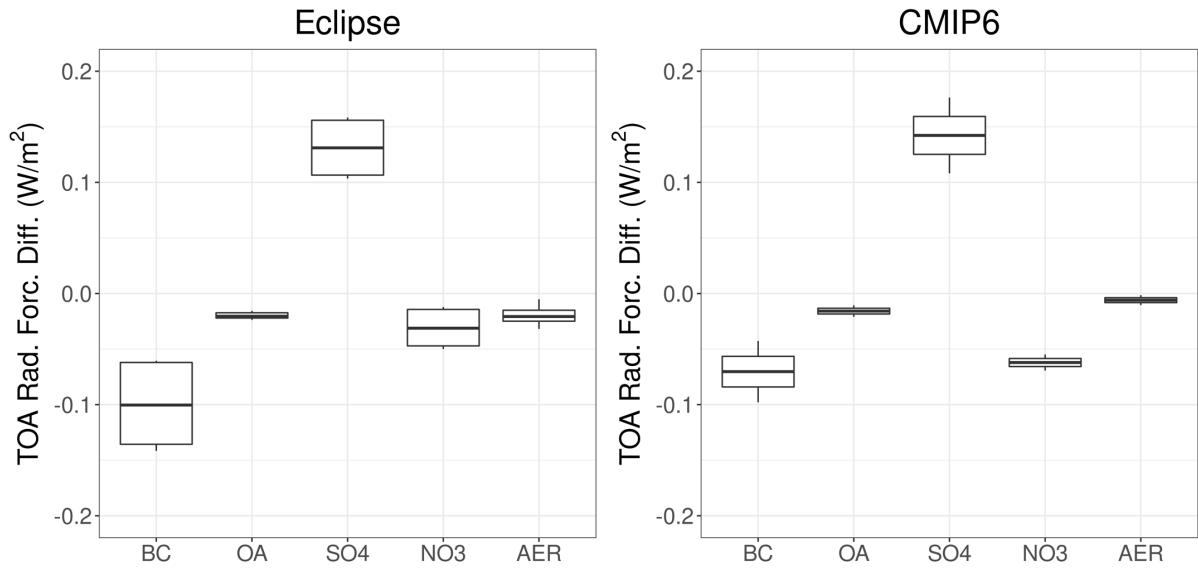
Figure 8. Box-Whisker plot showing the differences between 1990-2010 mean and 2030-2050 mean $RF_{ARI}$ for the anthropogenic aerosol components (BC, OA, $SO_4^{2-}$ and $NO_3^-$) and their sum (AER) in the Eclipse ensemble (CLE and MFR: left panel) and the CMIP6 (SSP2-4.5 and SSP1-2.6: right panel) ensembles. The boxes show the median, the 25th and 75th percentiles. The upper whisker is located at the *smaller* of the maximum value and $Q\_3 + 1.5$ IQR, whereas the lower whisker is located at the *larger* of the smallest x value and $Q\_1 - 1.5$ IQR, where IQR (interquartile range) is the box height (75th percentile - 25th percentile).
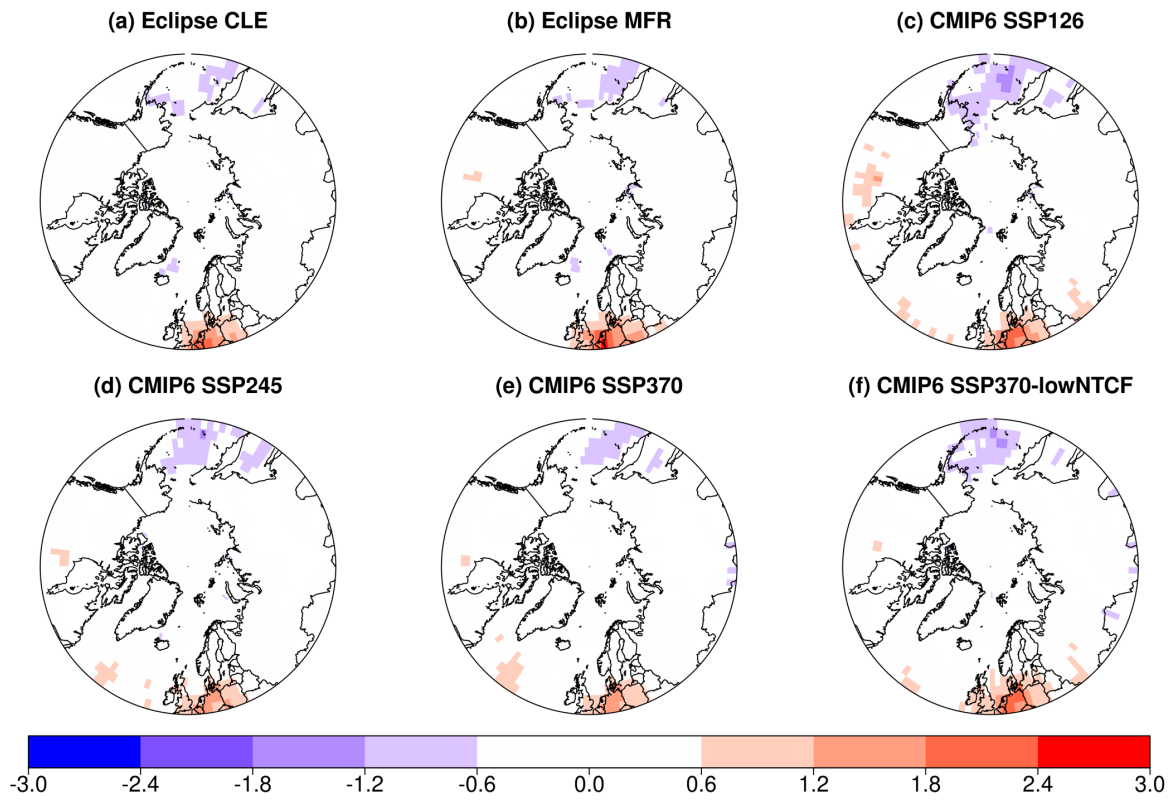
Figure 9. Spatial distribution of the statistically significant annual mean Arctic $RF_{ARI}$ (W m$^{-2}$) changes between the 1990-2010 mean and the 2030-2050 mean as calculated by the GISS-E2.1 ensemble.
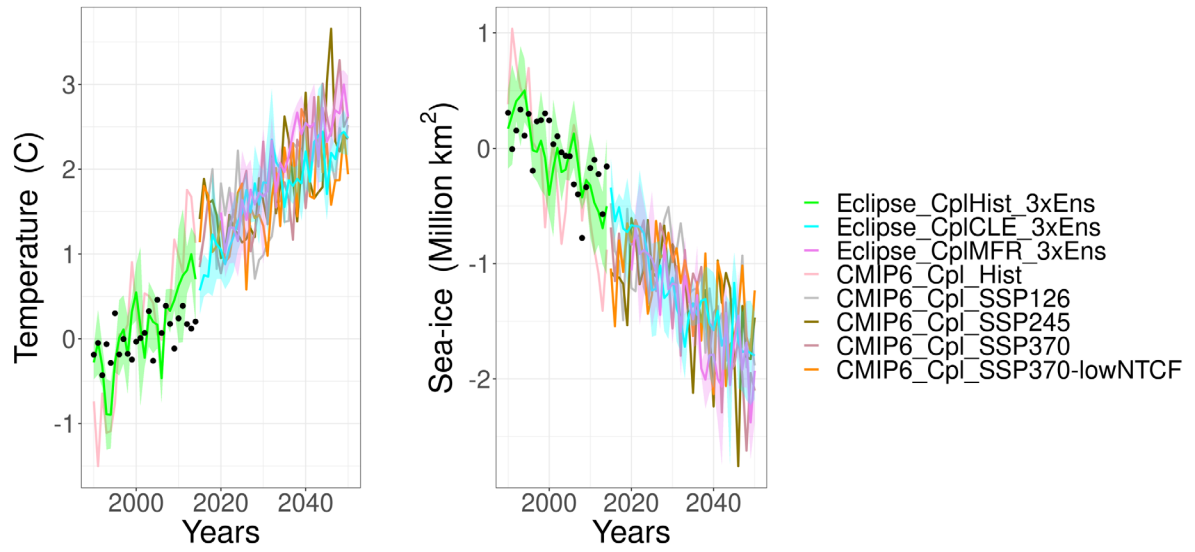
Figure 10. Arctic annual mean surface air temperature and sea-ice extent anomalies in 2015-2050 based on the 1990-2010 mean as calculated by the GISS-E2.1 ensemble.
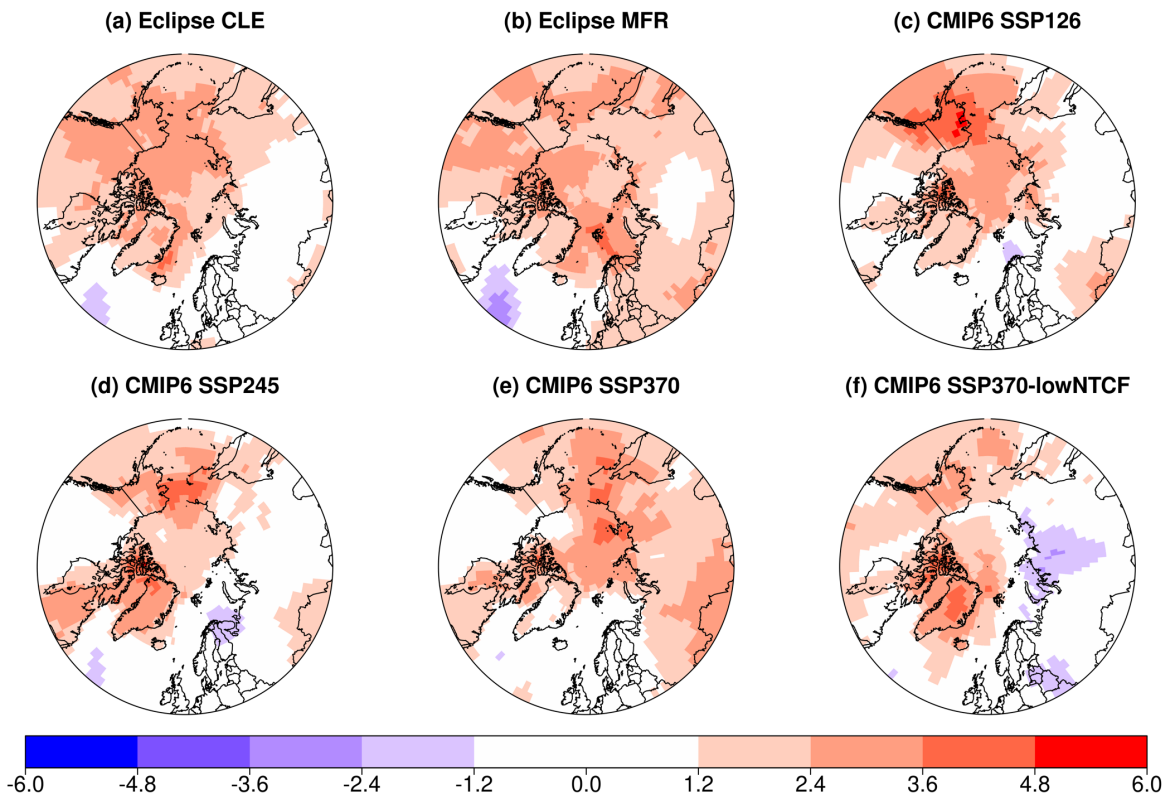
Figure 11. Spatial distribution of the statistically significant annual mean Arctic surface air temperature (°C) changes between the 1990-2010 mean and the 2030-2050 mean as calculated by the GISS-E2.1 ensemble.

**(a) Eclipse CLE**     **(b) Eclipse MFR**
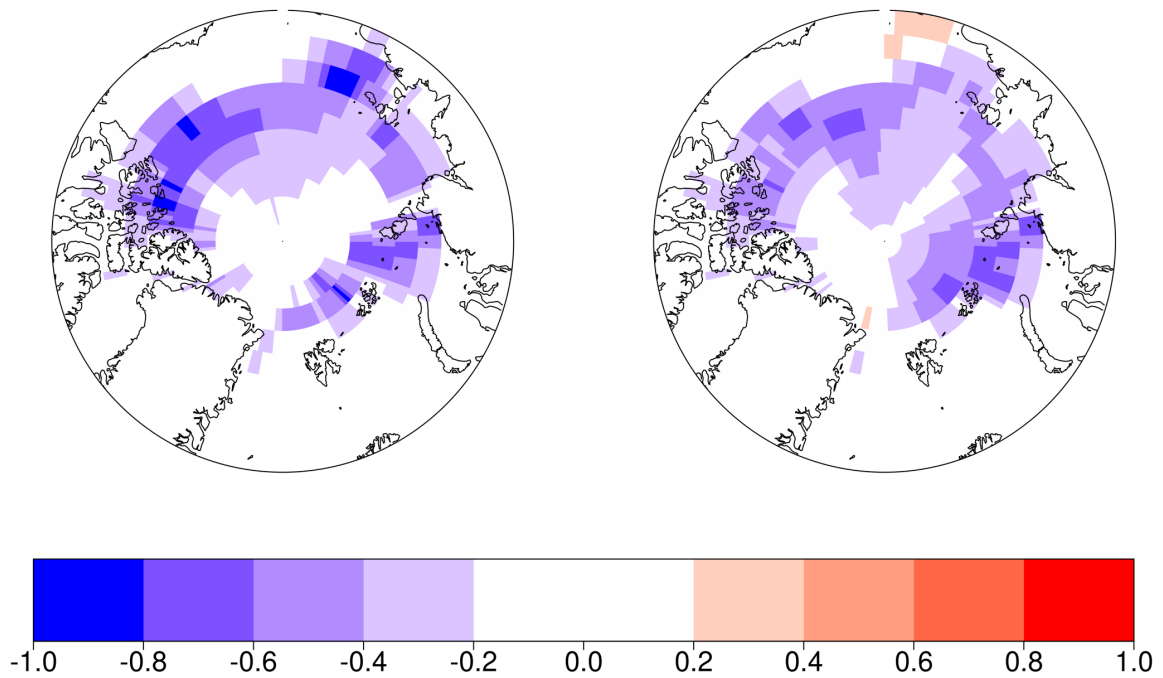
Figure 12. Spatial distribution of the statistically significant September Arctic sea-ice fraction change between the 1990-2010 mean and the 2030-2050 mean as calculated by the GISS-E2.1 Eclipse ensemble (CMIP6 ensemble is not shown due to statistically insignificant changes calculated by the student t-test).